Chirality-Induced Budding: A Raft-Mediated Mechanism for Endocytosis and Morphology of Caveolae?

R. C. Sarasij,*† Satyajit Mayor,† and Madan Rao*†

*Raman Research Institute, Bangalore, India; and †National Centre for Biological Sciences, Tata Institute of Fundamental Research-GKVK Campus, Bangalore, India

ABSTRACT The formation of transport carriers (spherical vesicles and tubules) involves membrane budding, growth, and ultimately fission. We propose a mechanism of membrane budding, wherein the tilt and chirality of constituent molecules, confined to a patch of area *A*, induces buds of ~50–100 nm that are comparable to vesicles involved in endocytosis. Because such chiral and tilted lipid molecules are likely to exist in "rafts", we suggest the involvement of this mechanism in generating membrane buds in the clathrin and dynamin-independent, raft-component mediated endocytosis of glycosylphosphatidylinositol-anchored proteins. We argue that caveolae, permanent cell surface structures with characteristic morphology and enriched in raft constituents, are also likely to be formed by this mechanism. Thus, molecular chirality and tilt, and its expression over large spatial scales may be a common organizing principle in membrane budding of transport carriers.

INTRODUCTION

The biogenesis of transport carriers involves membrane deformation, its growth into a spherical bud or tubule, and finally membrane fission (1). A special case of membrane traffic is displayed in endocytosis, the uptake of membrane proteins, lipids, and extracellular ligands from the cell surface. Endocytosis occurs in a wide range of cellular contexts with vastly differing requirements; cells appear to have evolved a diversity of pathways in terms of molecular mechanisms, regulation, cargo specificity, and kinetics (2,3). One such endocytic mechanism is the clathrin mediated (CM) pathway (4) responsible for the internalization of proteins such as transferrin (Tf) and particles such as low-density lipoproteins (LDL) that bind to specific transmembrane receptors on the cell surface. A large number of membrane deforming proteins such as clathrin, epsin, and dynamin, have been reported to be involved in CM endocytosis (3–6). However, even in this well-studied pathway, the physicochemical mechanism of membrane deformation and pinching are poorly understood (5).

Cell surface lipid-anchored proteins such as glycosylphosphatidylinositol (GPI)-anchored proteins (7,8) on the other hand, are endocytosed via an entirely different pathway. This pathway is responsible for the pinocytic (fluid-phase) uptake in many cell types from mammalian to insect cells, and does not involve the membrane deforming proteins of the CM-mediated pathway (7,9). Furthermore unlike the transmembrane cargo of the clathrin-mediated pathway, GPI-anchored proteins do not have any cytoplasmic extension to link with other cytoplasmic proteins involved in the formation of the appropriate carrier. Interestingly, GPI-anchored protein trafficking can be regulated by altering levels of cellular lipids, specifically cholesterol and sphingolipids (10,11).

We have recently shown that lipid-anchored proteins such as GPI-anchored proteins are organized in nanoscale, cholesterol-dependent clusters. This clustering is necessary for GPI-AP endocytosis (12–14). Combined with the experimental evidence that the preexisting lipidic organization of GPI-anchored proteins is actively maintained in the cell, it is likely that these clusters are induced to form larger domains that are endocytosed (14). These active large-scale domains represent specialized lateral heterogeneities in the membranes, similar to the hypothesized membrane rafts, enriched in cholesterol and sphingolipids (15–17).

The absence of any of the conventional membrane deforming proteins (dynamin, clathrin, and caveolin, eps15) (9), raises an important issue regarding the mechanism of endocytosis of GPI-anchored protein containing domains, or rafts. Most importantly, how does initiation of membrane curvature of the desired length scale, a necessary precursor to vesiculation, take place?

In providing a physical mechanism for raft-assisted cellular budding, we need to address the question of the mechanics of membrane deformation at larger than molecular scales, i.e., at mesoscopic scales. Why is membrane deformation a mesoscopic scale phenomena? Consider, for example, a typical domain of diameter 100 nm on a flat membrane, which is subject to mechanical deformation resulting in a bud. Such a patch would consist of $\sim 10^3$–10^4 lipids. At this scale, membrane deformation can be analyzed using continuum elasticity (18). Typical energy scales for membrane deformation, for example, leading to a clathrin-coated bud, are in the order of 10–20 k_BT at room temperature. Therefore, to create the required deformation, a collection of force centers is necessary; budding is a result of a collective property of its constituent molecules (which in general include lipids and membrane deforming proteins). One of the aims of our theoretical study is to identify molecular features that are

Submitted April 8, 2006, and accepted for publication October 19, 2006.

Address reprint requests to Madan Rao, E-mail: madan@rri.res.in.

0006-3495/07/05/3140/19 $2.00

doi: 10.1529/biophysj.106.085662

relevant for membrane shape, and consequently to membrane budding.

The specific lipid content of the raft (15–17,19) is sphingolipids (Sph), glycosphingolipids (GlySph), and cholesterol (Ch); these lipids are associated with the constitutive trafficking of GPI-anchored proteins (10,11). In this context, we can catalog those lipid aspects that may be relevant at the scales of the budding membrane patch: i), the stiffness of the long, saturated acyl chains leading to a high packing fraction below the main transition, T_m, the so called *lo* (liquid ordered) phase; ii), the presence of dipole moments on the headgroup; iii), the relative area of the head to the tail; iii), the presence of hydrogen bonding centers; and iv), lateral and transbilayer lipid heterogeneity. Here we argue that these molecular properties on their own, when coupled with membrane deformation produce bud sizes much larger than the typical endocytic buds.

Another molecular feature of the lipid constituents in the raft is their chirality. Chirality is the absence of mirror symmetry—a chiral molecule is one whose mirror image is a different molecule albeit of the same chemical composition (20). Indeed most molecules in the plasma membrane are chiral. However, molecular chirality needs to be expressed at larger scales to affect membrane shape.

Here we report that the special constitution and physical characteristics of rafts could promote the presence of a collective ''orientation or tilt field'' that is responsible for the expression of molecular chirality over the scale of the raft. This in turn leads to membrane shape deformations such as budding and tubulation. Using reasonable parameter estimates, it is possible to obtain bud sizes in the order of 50 nm (21). We suggest that the origin of the orientational field in rafts may be either a single molecular property such as molecular tilt (chain tilt or headgroup orientation) (22) of specific raft lipids, or a collective property such as the formation of chemical aggregates of the raft-associated cholesterol and sphingolipids, or nanoscale clusters of GPI-anchored proteins (13).

In addition to the simple spherical or tubular buds discussed above, we find that the taxonomy of membrane shapes arising from this interplay between orientation, chirality, and membrane elasticity includes novel ''flask-like'' and ''grape-like'' structures. These shapes show a remarkable similarity to caveolae that are permanent cellular invaginations at the surface of most eukaryotic cells (23). Caveolae are rich in raft lipids such as cholesterol and sphingolipids. We show that the conditions that promote such morphologies are consistent with the phenomenology of caveolae.

In summary, chirality, a common feature of membrane components, in conjunction with a tilt field can be expressed over large enough scales to induce membrane budding. Such a mechanism can result in bud sizes comparable with typical endocytic buds. We suggest that chirality-induced budding may be a common theme for membrane budding in different cellular contexts.

INADEQUACY OF CONVENTIONAL MECHANISMS OF BUDDING OF RAFT COMPONENTS ON THE CELL SURFACE

We discuss here the conventional physical mechanisms for membrane budding that incorporate some features of the specific lipid content of the raft, such as sphingolipids and cholesterol. These mechanisms involve an interplay between line tension, curvature elasticity, and spontaneous curvature. In the context of rafts, the justification for line tension induced budding (24–26), is based on the observation that in artificial membranes (freely suspended mono- and bilayers and giant unilamellar vesicles) containing a mixture of raft components Sph/Ch/PC, sphingolipids and cholesterol phase segregate from the rest over a wide range of temperatures (~40°C) and composition (~1:1:1), leading to macroscopic domains enriched in either Sph/Ch or the unsaturated PC, separated by sharp interfaces (27,28). The domains enriched in Sph/Ch were found to be in the liquid-ordered (*lo*) phase, characterized by higher packing fraction and stiffening of the hydrocarbon tails.

The tendency of the membrane to reduce the interfacial energy can lead to bud formation (24–26,29). In addition, budding can be facilitated and directed by the presence of a spontaneous curvature, an asymmetry between the two leaves of the bilayer, arising, for instance, because sphingolipids reside only in the outer leaflet of the plasma membrane. Any lateral segregation of these lipids on the outer leaflet, will automatically lead to a transverse lipid heterogeneity resulting in a local spontaneous curvature of the membrane. Local spontaneous curvature effects may also be augmented by the presence of cytosolic membrane bound proteins (e.g., caveolin (30)) and the cytoskeletal cortex.

Consider the simplest case of a raft domain P of area $A = \pi R^2$ and perimeter L on the outer leaflet of a tensionless membrane (Fig. 1); this domain contains specific lipids that are distinct from the rest of the membrane P'. The energy of such a membrane can be written as,

$$E = \sigma_0 L + \frac{\kappa}{2}\int_P (H - H_0)^2 dA + \frac{\kappa'}{2}\int_{P'} H^2 dA, \qquad (1)$$

where σ_0 is the line tension separating regions P and P', κ and κ' are the corresponding bend elastic moduli and H, the local mean curvature (definitions in Appendix A). For simplicity, we have ignored a possible Gaussian curvature contribution. The spontaneous curvature H_0 is a measure of the asymmetry in the lipid composition of the inner and outer leaflets in the region of the patch. We allow the conformations of the membrane to vary from a flat membrane with a circular domain of perimeter $L = 2\pi R$ to a spherical bud attached to the rest of the flat membrane via an infinitesimal neck, keeping the area A fixed.

First, drop the spontaneous curvature H_0, and let $\kappa = \kappa'$. Ignoring the negligibly small curvature energy contribution coming from the neck, we find, as first shown in Lipowsky

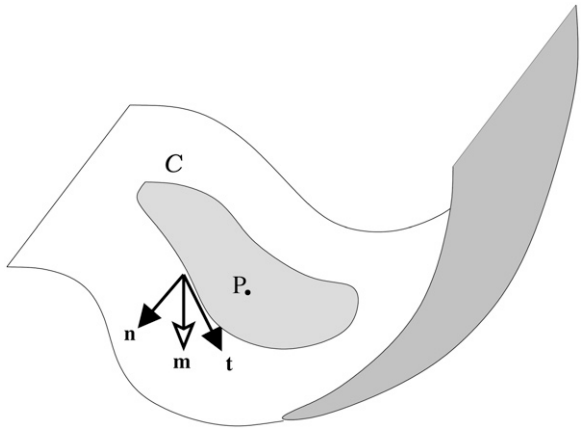

FIGURE 1 A raft-patch P decorated by a chiral tilt texture is bounded by a curve $\mathcal{C}$ on the outer membrane. The unit vectors **n** and **t** represent the normal and tangent to the boundary $\mathcal{C}$.

(24), that if R is greater than a threshold, the membrane forms a spherical bud; this provides a minimum bud size $r_{\text{bud}} = \kappa/\sigma_0$. To estimate its magnitude, we need to determine the values of the elastic parameters in the raft region of the plasma membrane. A more practical approach is to take the values measured in artificial systems that best resemble the lipid composition of rafts on the cell surface.

The section ''Estimation of parameters'' contains a discussion of estimates of the parameters involved in membrane deformation, from which we take the following values: $\kappa = 4 \times 10^{-19}$ J for a mixture of dimyristoylphosphatidylcholine (DMPC) with 50 mol % cholesterol (resembling the local concentration of cholesterol in the putative rafts) at 40°C, and $\sigma_0 \approx 10^{-13}$ N in giant unilamellar vesicles (GUVs) containing unimolar mixtures of Sph/Ch/PC.

These estimates give a minimum bud size $r_{\text{bud}} \sim 4\ \mu$m, at least two orders larger than in vivo bud sizes! In fact, it could be argued that this is an underestimate, because: a), we expect ''compatible'' nonraft lipids to organize proximal to the raft boundary, thus reducing σ_0; b), the coupling of the plasma membrane to the cortical proteins such as actin or other coat proteins would stiffen the membrane further; and c), the special *lo* nature of the segregated raft lipids would be accompanied by an increase in membrane thickness (31) and an enhanced splay stiffness; both these effects would lead to an increase in κ.

The estimate of the bud size could be reduced to some extent by transbilayer membrane asymmetries leading to a spontaneous curvature H_0 or alternatively to a relative extension of the inner membrane leaflet with respect to the outer. Spontaneous curvature can arise from the transverse asymmetry of raft lipids, coupling to a variety of raft proteins and receptors (e.g., the GPI-anchored proteins), or a strong coupling to cytoplasmic proteins. However, given that there are several integral and peripheral proteins that bind onto either side of the membrane raft (32), it is difficult to ascribe a unique nonzero magnitude and sign to the spontaneous curvature. Relative areal extension of the two leaves of the bilayer can arise from incorporation of excess lipids onto one leaf, e.g., (33), as a result the membrane can form a high curvature bud to accommodate this increase in relative tension.

In the context of curvature generation in caveolae that share the same raft composition, it has been argued (30) that the binding of the cytosolic membrane protein caveolin to the inner leaflet membrane via cholesterol, produces bending moments on the membrane leading to a spontaneous curvature. Starting with a tension-bearing membrane, these authors explicitly compute the deformation of a membrane arising from a model of force distribution generated by the binding of the caveolin oligomer to the membrane (30). With their numerical estimates, they find that $r_{\text{bud}} \approx 60$ nm, comparable to the radius of caveolae. However, they do not differentiate between spherical buds and flask-shaped invaginations, nor do they account for the grape-like or tubular morphologies that are unique features of caveolae (34).

One problem with these mechanisms and estimates is that they largely ignore the special molecular features of the raft constituents, namely its *lo* organization. Both an increase in the local bilayer thickness (31), and an increase in the splay energy arising from the *lo* nature of raft lipids should go against the tendency to bud, since both effects lead to an enhancement of the effective κ.

Undeniably, contributions from these mechanisms are present in any budding context that involves lateral and transverse lipid heterogeneity. However, the numbers that emerge suggest that these mechanisms on their own cannot produce buds of the required dimension (50 nm) and morphology (e.g., grapes and tubules). This suggests that we need to look for additional bulk contributions to membrane deformation energy that are specific to the lipid composition of rafts. Moreover this mechanism should produce different morphologies observed in the context of specific raft lipid containing caveolae. In the following sections, we provide an explanation of why the interplay between an orientational field and chirality, characteristic features of raft components, may produce membrane deformation leading to a bud (21). We also present a detailed study of the morphology of membrane shapes that are generated by these interactions.

''RAFTS'': A MEMBRANE PATCH INVOLVING ORIENTATION AND CHIRALITY

As discussed in the Introduction, raft components can be brought together either as a result of: i), macro phase segregation; ii), micro phase segregation (a long-lived equilibrium fluctuation) or (what is most likely); iii), an active organization at the cell surface (13,14). In this article we do not discuss the mechanism by which a ''raft'' membrane domain arises; instead we wish to understand the properties of raft lipids that could induce membrane curvature. For this we need to understand in greater detail, the molecular

specificity and the nature of interactions between the raft components. Sphingolipids have long saturated acyl chains (as does the GPI anchor) attached to a small sphingosine head that has an amide group and a (zwitter-)dipole moment. Cholesterol is a short stiff amphiphile with a hydroxyl group at the head. Glycosphingolipids, another raft component, is a type of sphingolipid attached to a large sugar group oriented along the plane of the membrane. All these molecules are strongly chiral.

Although the organization of raft components in live cells has not yet been elucidated, several experiments on artificial membrane systems containing ternary mixtures of Sph/Ch/PC, over a range of temperatures, pressures, and composition (27,28,35), suggest that membrane regions enriched in sphingolipids and cholesterol may be identified with a liquid-ordered (*lo*) phase with high packing density (27,28). This is supported by x-ray diffraction (36) and NMR studies (37), which suggest that the sphingolipid acyl chains in the *lo* phase are stretched out, thus reducing chain-entropy and increasing the local packing density. Atomic force microscopy of suspended mono-/bilayers (31), has revealed that membrane regions identified with the *lo* phase have larger membrane thickness by ~0.8 nm.

We suggest that active processes on the cell surface (14), primarily arising from cortical actin and other coat proteins, can give rise to a collective orientational field within the raft domain at the cell surface. For instance, cortical actin or coat proteins associated with raft regions can produce lateral stresses on the membrane bilayer, and thus modulate (decrease) the local bilayer thickness, inducing a tilt of the stiff acyl chains of the *lo*-raft lipids (S. Mayor and M. Rao, unpublished data). As is customary practice in liquid crystal physics, we denote the tilt version of the liquid-ordered phase by *lo′*. Alternatively, one may assign a tilt or bond orientation field with the cortical actin or coat proteins associated with rafts.

Whatever the origin of tilt or orientation, its presence on the raft domain immediately implies that local shape of the membrane should be governed by the coupling between tilt and curvature. This is borne out from numerous theoretical and experimental studies on artificial membranes (we provide relevant references as we go along). In addition, since the raft constituents are chiral, the existence of a well-defined orientational field allows this chirality to be expressed over the scale of the raft domain. This implies that local shape of the membrane should be governed by an interplay between chirality, tilt, and curvature. We will show that this is indeed the case; the interplay between chirality and orientation-curvature coupling (21) gives rise to a variety of membrane shapes such as buds, tubules, flasks, and grapes.

DESCRIPTION OF A MEMBRANE CONTAINING ORIENTATION AND CHIRALITY

In this section, we describe the deformation energy of a bilayer membrane containing a patch of raft-components (cholesterol+sphingolipids+glycosphingolipids) of fixed area on the outer leaflet, whereas the rest of the outer membrane and the inner membrane contains the phospholipids such as DMPC in the liquid-disordered phase. As discussed in ''Rafts: a membrane patch involving orientation and chirality'', the raft components can be represented by an orientational field with chiral interactions. Thus the deformation energy can be described in terms of a local orientational order and the local membrane morphology. If the orientation is associated with rigid molecular tilt, then it may in general be described by a polar vector that takes values in S^2 (Heisenberg spin) (38). However, (free)-energy considerations, a combination of hydrophobicity, van der Waals, and ''hydrophobic shielding'', constrain the center of mass of the molecules to lie on the two-dimensional (2D) membranal surface. Further the projection of the long axis of the molecule onto the 2D plane will have a fixed magnitude, since deviations of the projection from this fixed value cost a similar energy. Thus owing to strong uniaxial anisotropy, the orientational field at every point on the raft-patch may be described by a 2D polar vector $\mathbf{m}$ with unit magnitude (*XY* spin) (38). We will assume that within the raft-patch, the center of mass density $\rho(x, y)$ is uniform.

The raft-components interact with each other, and with the molecules outside the patch, both sterically (purely repulsive) and via short-range (e.g., van der Waals) attractive interactions. Both these effects contribute to chiral interactions; the former via the Straley picture of interlocking screws (39), the latter via a generalization of the Van der Waals dispersion to chiral molecules (40). In the continuum limit, these short-range interactions can be written as the usual Frank energy (41), modified to include the effects of chirality.

Of course, in addition to these short-range interactions there could be long-range dipole-dipole (or higher multipole) interactions between the tilt molecules carrying a permanent dipole moment. The long-ranged quadrupolar (or higher multipolar) interactions may also have independent chiral contributions. However, in this article, we will largely ignore the contribution of dipolar interactions, which we justify in ''Estimation of parameters'' by demonstrating that they are smaller than the Frank energy contributions.

Though the system of rafts embedded in the cell membrane may not be in thermodynamic equilibrium, we will assume that a single raft, taken to be a stable circular region of area A on the membrane, attains a conformation minimizing the free energy of that single raft (Fig. 1). This assumption tacitly entails another: variations in the size of the raft due to molecules leaving and entering the raft, either via diffusion or exo/endocytosis, are small compared to A. Furthermore, all macroscopic quantities associated with the raft, such as its energy, its texture, or its shape, are evaluated not at a single instant of time but are averaged over a timescale long compared to the timescale of variations in A, but shorter than endocytic or domain coalescence timescales of seconds to tens of seconds.

Energy functional describing the raft

Recalling that the raft components are on the outer leaflet of the cell membrane, our description of the bilayer membrane thus starts with a membrane patch of area A on the outer leaflet decorated by an orientation field $\mathbf{m}$, the inner lipid leaflet being structureless. We then project these variables onto the neutral surface of the membrane (42), represented as a mathematical surface $\vec{R}(x_1, x_2)$. Each leaflet has its own elastic stiffness; combining the sheets, the elastic stiffnesses simply add (for this asymmetric bilayer). The raft will thus be a (simply or multiply connected) domain with perimeter L (which is allowed to vary) on this neutral surface. The conformation of the domain is described by the local texture $\mathbf{m}$, the local membrane shape $\vec{R}(x_1, x_2)$, and the boundary $\mathcal{C}$. (We will consistently denote 2-vectors with boldface and 3-vectors with an over-arrow.)

The effective energy-functional written in terms of $\mathbf{m}$ and the local membrane curvature K_{ij} (see Appendix A for mathematical definitions) may be divided into contributions from within the patch (P), the boundary ($\mathcal{C}$), and outside the patch (P'),

$$E[\mathbf{m}, \vec{R}, \mathcal{C}] = E_{\mathrm{P}}[\mathbf{m}, \vec{R}] + E_{\mathcal{C}}[\mathbf{m}, \vec{R}, \mathcal{C}] + E_{\mathrm{P}'}[\vec{R}]. \quad (2)$$

The energy functional within the patch has contributions from distortions of the orientation $\mathbf{m}$ (written as a generalized Frank energy), deformations of the shape of the membrane (written as a Helfrich energy), and a coupling between the curvature and the orientation.

$$E_{\mathrm{P}}[\mathbf{m}, \vec{R}] = E_{\mathrm{frank}} + E_{\mathrm{helrich}} + E_{\mathrm{coupling}}. \quad (3)$$

The form of the energy follows from general symmetry arguments (21,43–47); here we retain terms up to quadratic order in fields and to lowest order in spatial derivatives. The former restriction assumes that the field values are small, the latter says that we are interested in mesoscopic scale physics, at the scale of the bud. To ensure that we have accounted for all contributions to this order, we write the energy in a covariant form (21,45). The generalized Frank energy can be written as,

$$E_{\mathrm{frank}} = \int_{\mathrm{P}} \sqrt{g} d^2x \left[\frac{k_1}{2} (\mathrm{Div}\, \mathbf{m})^2 + \frac{k_2}{2} (\mathrm{Curl}\, \mathbf{m})^2 + k_{\mathrm{c}} (\mathrm{Div}\, \mathbf{m})(\mathrm{Curl}\, \mathbf{m}) + \sigma_1 (\mathrm{Div}\, \mathbf{m}) + \sigma_2 (\mathrm{Curl}\, \mathbf{m}) \right]. \quad (4)$$

The generalized splay and bend terms are defined via the covariant divergence (Div) and curl (Curl) of a vector field $\mathbf{m}$ on a curved surface (Appendix A). For simplicity, we will assume the equal-constants approximation where $k_1 = k_2 = k$. Note that for a 2D vector field $\mathbf{m}$, Curl $\mathbf{m}$ is a pseudoscalar: the k_{c} and σ_2 terms are chiral and so are dependent on the density of the chiral molecular component.

The membrane deformation energy is written in the usual Helfrich form (48),

$$E_{\mathrm{helfrich}} = \int_{\mathrm{P}} \sqrt{g} d^2x \left[c_0 H + \frac{\kappa}{2} H^2 + \frac{\bar{\kappa}}{2} K \right], \quad (5)$$

where the mean curvature H and the intrinsic (Gaussian) curvature are the trace and determinant of the local curvature tensor $K^{\mathrm{j}}_{\mathrm{i}}$ (Appendix A). For convenience, we have assumed that the membrane has zero bare surface tension. The coupling between the texture and curvature is given by

$$E_{\mathrm{coupling}} = \int_{\mathrm{P}} \sqrt{g} d^2x \left[\beta m^{\mathrm{i}} m^{\mathrm{j}} K^{\mathrm{i}}_{\mathrm{j}} + c_0^* \gamma_{\mathrm{ij}} m^{\mathrm{k}} m^{\mathrm{i}} K^{\mathrm{j}}_{\mathrm{k}} \right], \quad (6)$$

where the last term is pseudoscalar (chiral), as indicated by the presence of the totally antisymmetric tensor γ_{ij} (Appendix A), and is referred to as the Helfrich-Prost interaction (49). In addition, there are anisotropic bending terms, such as $(\mathbf{m}\cdot K \cdot K \cdot \mathbf{m})$ and $(\mathbf{m}\cdot K \cdot \mathbf{m})^2$ (50,51), which can lead to the formation of spherical buds and tubules on their own, i.e., without the help of chirality. We have however ignored such contributions since they are higher order in wavenumber and fields.

The contribution from outside the patch P' is given by

$$E_{\mathrm{P}'}[\vec{R}] = \int_{\mathrm{P}'} \sqrt{g} d^2x \left[\frac{\kappa'}{2} H^2 + \frac{\bar{\kappa}'}{2} K \right]. \quad (7)$$

In general, the elastic moduli $\kappa, \bar{\kappa}$ are different in regions P and P'. In our variational calculation we will for the most part assume that membrane in P' is flat (or asymptotically flat) and that all shape variations are restricted to the region P. We will also ignore the contribution of the Gaussian curvature term.

The boundary energy is proportional to the perimeter of the boundary $L(\mathcal{C})$, with a line tension σ_0,

$$E_{\mathcal{C}} = \sigma_0 L(\mathcal{C}). \quad (8)$$

Note that the total derivative terms Div and Curl in Slepnev and de Camilli (4) can be integrated to the boundary via a generalized Gauss and Stokes law (52); this will give rise to an anisotropic line tension. For simplicity we will fix the boundary to be a circle on the flat membrane surface P', take only the isotropic tension, and, ignore a potential geodesic curvature contribution to the boundary energy.

Given the total energy functional, we obtain the optimal conformation of the membrane shape and texture that minimizes this energy, subject to two constraints. One is that the orientation $\mathbf{m}$ is a unit vector—this may either be ensured by a ''hard-spin'' version of the model (where we explicitly set $|\mathbf{m}| = 1$, by suitable parameterization) or a soft-spin potential of the form $V(\mathbf{m}) = -\alpha(\mathbf{m}\cdot\mathbf{m}) + \beta(\mathbf{m}\cdot\mathbf{m})^2$, which makes deviations of $|\mathbf{m}|$ from unity hard to obtain.

A note of caution—our restriction to terms with lowest order in spatial derivatives is valid only when the length scale over which the deformation occurs is large. To check whether this restriction is valid over scales corresponding to the bud size, we have explicitly considered the contribution of symmetry allowed terms containing higher order spatial

derivatives such as, $(\mathbf{m}\cdot K\cdot\mathbf{m})(\mathrm{Div}\ \mathbf{m})$, $K_{\mathrm{i}}^{\mathrm{j}}(\mathrm{Div}\,\mathbf{m})$, $K_{\mathrm{i}}^{\mathrm{j}}(D_{\mathrm{i}}m^{\mathrm{j}})$, $m^{\mathrm{k}}K_{\mathrm{ki}}m^{\mathrm{j}}(D_{\mathrm{j}}m^{\mathrm{i}})$, and a chiral contribution $(K_{\mathrm{i}}^{\mathrm{i}})(\mathrm{Curl}\ \mathbf{m})$. We find them to be smaller than the terms retained; indeed the effect of these terms (except the chiral term) is to renormalize the spontaneous curvature c_0 and β, favoring the formation of a bud.

Before ending this section, we restate that the parameters in front of the chiral terms in the energy functional, principally k_{c} and c_0^* are nonzero only when the constituent molecules are chiral. They are phenomenological parameters that may vary with temperature, concentration, and surface pressure, and may even change sign (40).

PHASE DIAGRAM: TEXTURE AND SHAPE

We take a variational approach (21) to obtain the optimal shape and texture—this involves: i), guessing the right conformation; ii), expressing the conformation by a few parameters; and iii), obtaining the optimal values of the parameters. Most often our guesses are based on symmetry considerations and a general understanding of chiral structures; in some cases, however, they are guided by Monte Carlo simulations. Because our aim is to understand the nature of budding induced by chirality, we will simplify our energy functional and focus particularly on the effects of chirality.

Without loss of generality, we may set our units of length and energy such that $k = 1$ and $\sigma_0 = 1$.

Before we examine the effects of chirality on a deformable membrane, it is instructive to study finite chiral textures in the rigid ($\kappa \to \infty$) limit where the membrane is a flat 2D plane.

Texture on a flat membrane

In the case of a flat membrane, the form of the energy functional is considerably simplified (21,53–55). Keeping only the isotropic tension, we can rewrite the Frank energy functional (4) as

$$E_{\mathrm{flat}} = L + \int_{\mathrm{P}} \frac{1}{2}(\mathrm{div}\,\mathbf{m} + \mathrm{curl}\,\mathbf{m})^2 + (k_{\mathrm{c}} - 1)(\mathrm{div}\,\mathbf{m})(\mathrm{curl}\,\mathbf{m}). \quad (9)$$

Increasing the chiral strength, $k_{\mathrm{c}} > 1$ (in units of Frank constants), the raft would assume a texture with a high curl and a divergence equal and opposite to the curl. Such a condition is satisfied by the Archimedes spiral texture (Fig. 2 *a*), where the lines of $\mathbf{m}$ diverge from the center C. In polar coordinates (r, θ) with the origin being at the center of the raft, the spiral described by $\mathbf{m} \equiv (m_{\mathrm{r}}, m_\phi)$,

$$m_{\mathrm{r}}^2 + m_\phi^2 = 1 \quad (10)$$

$$\mathrm{div}\,\mathbf{m} = \frac{m_{\mathrm{r}}}{r} \quad (11)$$

$$\mathrm{curl}\,\mathbf{m} = \frac{m_\phi}{r}, \quad (12)$$

has constant radial and tangential components everywhere in the raft. This spiral texture is optimized by $m_{\mathrm{r}} = 1/\sqrt{2}$, $m_\phi = -1/\sqrt{2}$, where the lines of $\mathbf{m}$ diverging from the center C, subtend an angle $\pi/4$ with respect to the local radial direction. The energy of this optimal texture is

$$E_{\mathrm{flat}} = 2\pi R - \pi(k_{\mathrm{c}} - 1)\ln\frac{R}{r_{\mathrm{c}}} + \epsilon_{\mathrm{c}}, \quad (13)$$

where $R = \sqrt{A/\pi}$ is the radius of the raft, r_{c} and ϵ_c are the core radius and core energy of this spiral defect. The chiral energy density is large (and negative) in the vicinity of the core, and falls off as r^{-2}.

As k_{c} increases, the texture prefers to place such high chirality regions all over the domain. Using a Monte Carlo simulation with simulated annealing (21,55), we showed that a chiral tweed texture, with the above characteristic (Fig. 3), wins over the spiral defect phase. We were then able to parameterize this texture and calculate its energy analytically. This gives the phase diagram Fig. 4.

Texture and shape of a deformable membrane: budding and tubulation

We revert to the energy functional (2) when the membrane is deformable; the chiral interactions are now represented by two terms k_{c} and c_0^*. Before exhibiting a detailed phase diagram (21), we provide a qualitative understanding of the effects of these chiral terms on the shape and texture of the membrane.

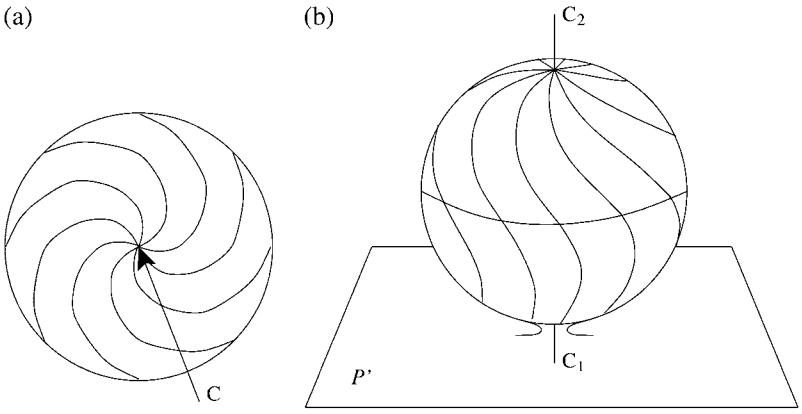

FIGURE 2 (*a*) Chiral texture on a flat membrane, the plane of the paper; *C* is the center of chirality. (*b*) A spherical bud induced by chirality, connected to the plane *P′* by an infinitesimal neck; C_1 and C_2 are centers of chirality.

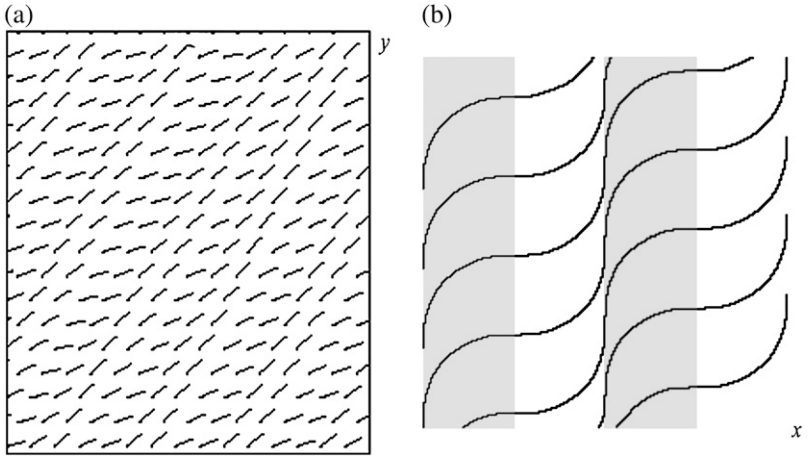

FIGURE 3 (*a*) Close-up of the texture generated by Monte Carlo simulation, (*b*) its continuum representation by a mathematical formula. In the shaded regions div **m** is positive and curl **m** is negative, whereas it reverses sign in the unshaded.

Start with $c_0^* = 0$: we have just shown that the optimal texture of a circular domain of radius R on a flat membrane when $k_c > 1$, is an Archimedes spiral diverging from the center of the domain (Fig. 2 *a*). If the membrane is made flexible, then the spiral can close itself on the opposite pole of a sphere, producing two centers of chirality, C_1 and C_2, instead of one (Fig. 2 *b*)—this conformation gains in both bulk chiral energy (Appendix B) and line tension energy. A spherical bud would be produced if the k_c contribution is sufficiently strong to overcome the rigidity of the membrane.

Now start with $k_c = 0$: as shown in (49) and explicitly demonstrated in Appendix B, a sufficiently large value of c_0^* would prefer to wrap the texture in a helix around a narrow cylinder, the pitch of the helix being proportional to the radius of the cylinder.

Thus the interplay between k_c and c_0^* will produce a combination of spherical caps and cylinders. Appendix B contains detailed calculations of the combined effects of k_c and c_0^* for textures on prescribed surfaces such as the sphere, cylinder, and saddle. These calculations help us in constructing general variational shapes (obtained by patching these surfaces) and textures (smoothly connecting the lines of **m**), which we optimize to obtain a detailed phase diagram. To highlight the effects of chirality we have ignored the spontaneous curvature c_0 of the raft. Including the effects of c_0 and β (Eq. 6) would enhance the tendency to form buds even further.

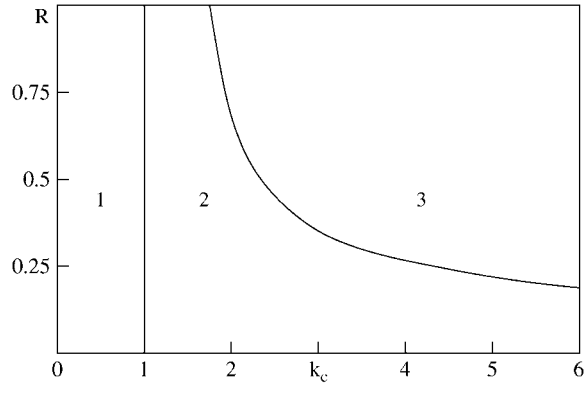

FIGURE 4 Phases of a chiral tilt-texture domain on a plane: (*1*) uniform phase, (*2*) spiral defect phase with $\epsilon_c = 0$, $r_c = 0.005$, (*3*) chiral tweed phase with stripe width $l^* = 0.01$.

We parameterize the spherical bud by a spherical cap of radius r_{bud} attached to the rest of the membrane by an infinitesimal neck of radius r_0. Using the parameterization of the texture **m** as given in Appendix B, we have calculated the optimum energy (texture+shape) for $c_0^* = 0$ variationally,

$$E_{sphere} = 2\pi r_0 + \pi\kappa\left(\frac{R}{r_{bud}}\right)^2 - \pi(k_c - 1)\int_{\theta_c}^{\pi-\theta_0} \frac{\cos^2\theta}{\sin\theta} d\theta + \epsilon_c + \epsilon_k, \tag{14}$$

where $\theta_c = r_c/r_{bud}$ is the angle subtended by the defect core of radius r_c at the center of the bud, and $\theta_0 = r_0/r_{bud}$ is the angle subtended by the neck at the center of the bud. The contributions ϵ_k and ϵ_c represent the energies of the neck and the defect core, respectively. Because the area of the domain is the same, before and after, the formation of the bud, we have,

$$A = \pi R^2 = 2\pi r_{bud}^2(1 - \cos\theta_0). \tag{15}$$

The chiral bulk energy k_c prefers to have zero neck radius, as seen from the variational calculation. This is because an infinitesimal neck allows the spherical bud to have two defects, resulting in a gain in chiral energy. Moreover, as $r_0 \to 0$, the neck energy $\epsilon_k \to 0$ (26,56). As we will see later, the Helfrich-Prost contribution, c_0^*, reduces the energy cost of the neck even further.

As we increase the value of c_0^* the bud is stretched into a prolate shape, with the defect drawn away from the neck. We represent this prolate bud by a cylinder of length l capped by two hemispheres of radius r_{bud} on either side, one of which joins the rest of the (flat) membrane via an infinitesimal neck. The **m** texture on the cylinder is the helix described in Appendix B, whereas the **m** texture on the sphere is the spiral described in Appendix B (and above). Note that the helical

lines of **m** on the cylinder smoothly join the spiral lines on each hemisphere. The energy of this prolate bud is

$$E_{\text{prolate}} = 2\pi r_0 + 2\pi\kappa(1+\cos\theta_0) - \pi(k_c-1)\int_{\theta_c}^{\pi-\theta_0}\frac{\cos^2\theta}{\sin\theta}d\theta + \epsilon_c + \epsilon_k + 2\pi r_{\text{bud}} l\left(\frac{\kappa}{4r_{\text{bud}}^2} - \frac{c_0^*}{2r_{\text{bud}}}\right). \quad (16)$$

We have numerically obtained the optimum shape and texture of the bud, with the constraint that the area of the bud

$$A \equiv \pi R^2 = 2\pi r_{\text{bud}}^2(1+\cos\theta_0) + 2\pi r_{\text{bud}} l, \quad (17)$$

remains the same on budding. A reasonable measure of prolateness of the bud is $(2r_{\text{bud}} + l)/2r_{\text{bud}}$; the prolateness increases sharply when c_0^* becomes of the order κ/R (Fig. 5 *b*).

Note that we have taken k_c and c_0^* to be positive everywhere; had they been negative we would simply reflect the optimal texture shown in Fig. 5 *a* on a mirror passing through the axis of the bud.

The variational calculation just outlined produces the phase diagram (Fig. 6), showing how a domain of size R on a flat membrane can give rise to a spherical/prolate bud or tubule by turning on the strength of chirality; the transitions are discontinuous. For instance, a domain of size $R = 0.01$ (corresponding to 10 nm) on a flat membrane can be induced to form a spherical bud as soon as $c_0^* = 75$, for $\kappa = 10$ and $k_c = 2$ (this, as we will see in the section ''Caveolae: a consequence of tilt and chirality?'' are perfectly reasonable estimates). Recall the lower bound $r_{\text{bud}} = 4\ \mu$m in the section ''Inadequacy of conventional mechanisms of budding of raft components on the cell surface''; the tendency to bud via bulk chirality preempts budding induced by line tension alone.

Fragmentation of a bud: maximal bud size

The phase diagram in Fig. 6, showing the discontinuous budding transitions, holds for small values of R. What happens when we increase the domain size R further, keeping all other parameters fixed? We will see that chiral interactions can induce a large enough domain to split into multiple domains.

That anything unusual should happen for larger domains may be gauged by the following argument (55). Consider a chiral tilt domain of radius R on a flat membrane with $\kappa \to \infty$. Because increasing the strength of k_c beyond unity produces a spiral defect at the center of the domain, we expect that when $k_c > 1$, the texture would prefer to maximize the number of spiral defect points. One way to achieve this is for the domain to split into multiple domains. To study the conditions under which such breakup is favorable, we calculate the energy $E_{\text{flat}}^{(n)}$ of n circular domains of equal area, each bearing the same spiral texture and compare it to the energy $E_{\text{flat}}^{(1)}$ of a single circular domain with the same total area and texture. The total energy of this configuration is

$$E_{\text{flat}}^{(n)} = 2\pi\sigma_0\sqrt{n}R - n\pi(k_c-1)\ln\frac{R/\sqrt{n}}{r_c} + n\epsilon_c. \quad (18)$$

For small values of R, a single domain $E_{\text{flat}}^{(1)}$ has the least energy. As R increases, $E_{\text{flat}}^{(2)}$ becomes smaller than $E_{\text{flat}}^{(1)}$: chirality in the bulk wins over interfacial energy. As R increases further, multidomain splitting is favored. This tendency to split holds when k_c is large enough; for a fixed value of $\sigma_0 r_c$, there is a critical k_c beyond which chirality-induced splitting would manifest. The relevance of this analysis to the observed domain repulsion in lipid domains on tense GUVs consisting of two lipid components has been discussed in Sarasij and Rao (55).

The above argument can be extended to bud splitting when the membrane is deformable. We find that as long as the chiral parameters k_c and c_0^* are large enough, the bud will prefer to split into two beyond a critical size. Assuming that the neck of the spherical bud attached to the parent membrane is infinitesimally small, we have for the total energy of n equal buds with the same texture,

$$E_{\text{sphere}}^{(n)} = 4\pi n\kappa - \pi n(k_c-1)\int_{\theta_c}^{\pi-\theta_c}\frac{\cos^2\theta}{\sin\theta}d\theta + 2n\epsilon_c. \quad (19)$$

This form assumes that the buds do not interact with each other. With a large chiral strength $k_c \gg 1$, we find that for small values of R, a single bud $E_{\text{sphere}}^{(1)}$ has the least energy. As R increases, $E_{\text{sphere}}^{(2)}$ becomes smaller than $E_{\text{sphere}}^{(1)}$: bulk chirality prefers the bud to split into two, when $R > R^*$ as seen in Fig. 7.

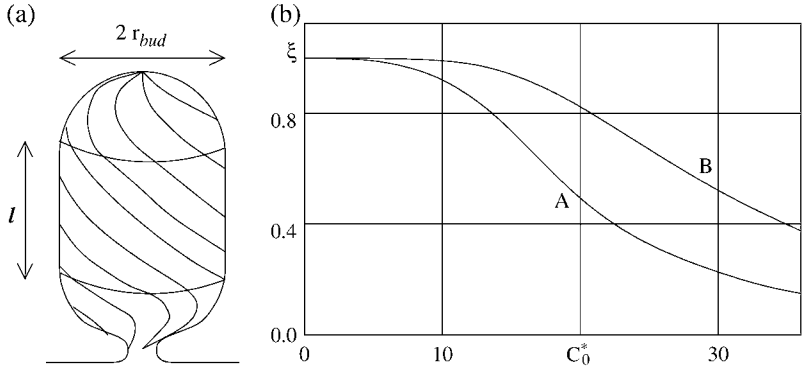

FIGURE 5 (*a*) Texture on a prolate bud, (*b*) measure of bud prolateness, $\xi = 2r_{\text{bud}}/(2r_{\text{bud}}+l)$, as a function of c_0^* for two different domain sizes (*A*) $R = 1$ and (*B*) $R = 0.5$. The rest of the parameters are: $\kappa = 10$, $k_c = 2$, $\epsilon_c = 0$, $r_c = 0.005$, $\epsilon_k = 0$, and $r_0 = 0.005$.

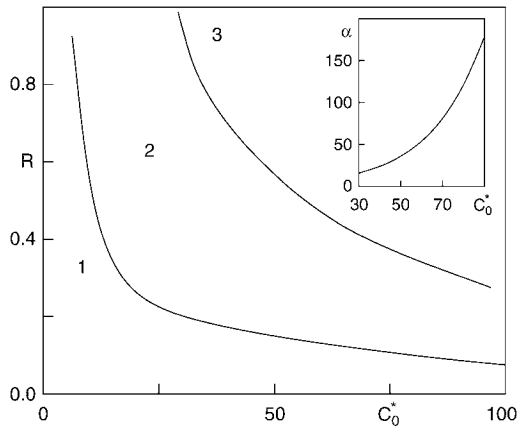

FIGURE 6 Phase diagram showing (*1*) planar, (*2*) spherical bud, and (*3*) cylindrical tubule, with $k_c = 1.5$, $\kappa = 10$. With these parameters, budding due to line tension alone (see ''Inadequacy of conventional mechanisms of budding of raft components on the cell surface'') occurs at $R = 10$. Inset shows the variation of the ratio $\alpha = L/r$ with c_0^* for a domain of size $R = 1$.

This tendency to split has interesting consequences for the growth of nucleating domains/buds. Consider two proximal domains on the membrane that have grown to a size R^*. Subsequent coalescence of these domains would be prevented by chirality; instead two spherical buds would emerge from the membrane surface. This would set a maximal bud size determined by the values of the chiral parameters. This is consistent with the sizes of buds involved in the GPI-anchored protein internalization pathway.

CAVEOLAE: A CONSEQUENCE OF TILT AND CHIRALITY?

To circumvent the splitting tendency of chirality so as to form large, stable raft domains on the membrane, we need additional molecular mechanisms to hold the raft together. Once this is achieved, we may ask what is the morphology of membranes when the size of the raft domain increases beyond R^*. The spherical/prolate buds and tubular shapes are only a subset of the energy minimizing shapes exhibited by this model. Rather than spanning the entire shape space, we take cues from other raft-associated structures on the cell surface.

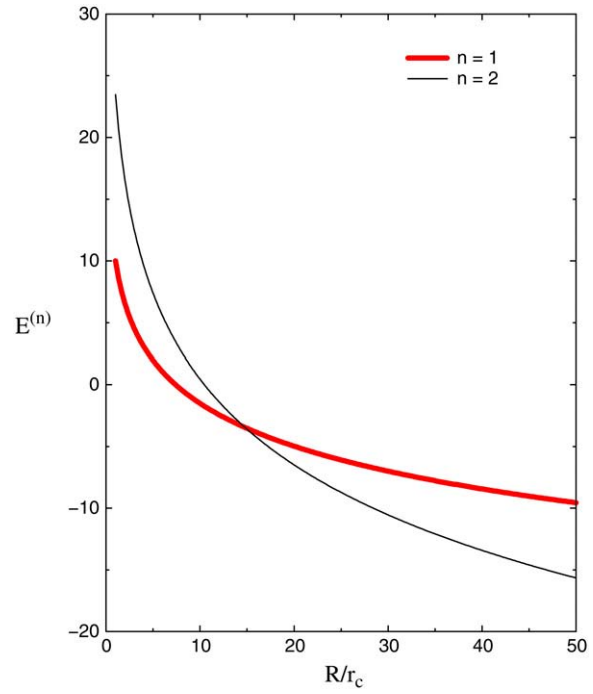

FIGURE 7 Energy $E^{(n)}$, of a bud split into n equal parts, depends on its total area, $A = \pi R^2$. Here we show the $n = 1$ and 2 branches: the bud prefers to split in two when $R > R^*$ ($\sigma_0 r_c = 1.5$, $\epsilon_c = 5$, $k_c = 17$).

The surface of most mammalian cells have stable cellular invaginations known as caveolae (34). Caveolae are rich in cholesterol and sphingolipids (57), and other raft constituents. They are morphologically distinct: large flask-shaped or ''grape-like'' invaginations on the plasma membrane, with a diameter nearly an order of magnitude larger than the size of the raft-assisted buds discussed earlier.

A defining feature of caveolae is the presence of caveolin, coat proteins that striate the cytoplasmic surface of caveolae. Caveolin binds to cholesterol and glycosphingolipids and is firmly anchored to the membrane by a palmitoyl chain (Fig. 8). Caveolins oligomerize on the membrane forming the characteristic spiral striations observed in freeze-fracture

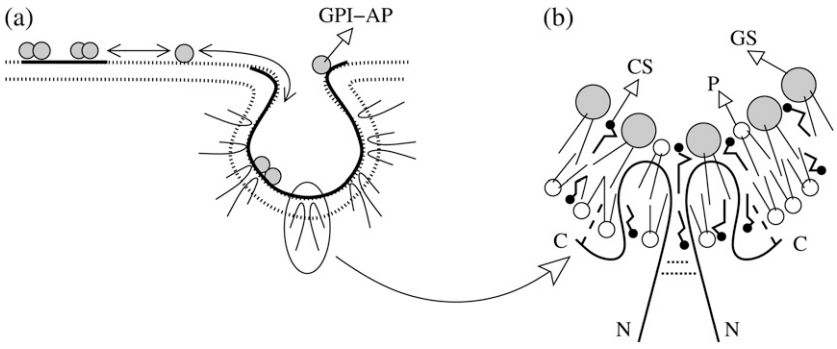

FIGURE 8 (*a*) Raft domains recruited into caveolae are held together by the oligomerization of the membrane bound protein, caveolin (represented by hairpins). (*b*) Close-up of a part of a caveola showing the oligomerization of caveolins (CS, cholesterol; GS, glycosphingolipids; P, phospholipids; C, carboxyl terminus, N, amino terminus). Horizontal lines between caveolins represent oligomerization, dashed lines near *C* represent palmitoylation (59).

images. It is likely that this ability to bind cholesterol and form oligomers helps sequester ''rafts'' into larger structures (58), thus stabilizing the caveolar pits (59). In our view, this binding due to caveolin oligomerization is the additional molecular mechanism needed to hold the raft together and make a domain larger. This novel role for caveolin is in addition to other effects that membrane-bound caveolin might have such as generating bending moments to curve the membrane (30).

In addition to the simple spherical/prolate/tubular buds discussed above, we indeed find that the taxonomy of membrane shapes include the ''flask-like'' (Fig. 9) and ''grape-like'' structures exhibited by caveolae. We show that these unique morphologies are favorable under conditions of: i), high chiral strength k_c and c_0^* (Fig. 10); ii), large raft area R (Fig. 11); and iii), high bending modulus κ (Fig. 12)—conditions that are characteristically met in caveolae.

Flask shapes

Caveolar flasks are round bottomed with a distinct neck, and so in our parameterization of the shape, we need to explicitly include the shape and texture of the neck. At first sight it might seem that including the neck portion would give a prohibitively large energy contribution to the bud; however, we will show that for high enough c_0^*, a neck is the favored conformation, i.e., $\epsilon_k \ll 0$.

We model the neck by patching together a saddle and a cylinder (Fig. 9). We have described the saddle geometry in Appendix A, and have seen that the texture favored by chirality (Appendix B) is the one in which the lines of $\mathbf{m}$ at any point bisect the right angle between the transverse and the longitudinal sections of the saddle passing through that point (see Fig. 15). The neck begins at the smallest cross section of the saddle, the circle $\mathcal{C}_\beta$ of radius R_β and angle $\alpha = 0$ and fans out to the maximum angle $\alpha = \alpha_{max}$, where the radius of the cross section is $R_\beta + R_\alpha(1 - \cos\alpha_{max})$ (Fig. 15).

A flask has two necks (Fig. 9): the first one connects the spherical part to the cylinder and the second connects the cylinder to the plane of the mother membrane. The spiral texture of the first neck merges smoothly with the texture of the cylinder on one side and with the texture of the sphere on the other. In a like manner the texture of the second neck merges smoothly with that of the cylinder.

The first neck subtends an angle θ_0 at the center of the sphere (Fig. 9), thus $\alpha_{max}^{(1)} = \theta_0$; further, as the neck joins up with the cylinder of radius R_C, we have $R_\beta{}^{(1)} = R_C$. If R_S is the radius of the sphere then from geometry,

$$\theta_0 = \arcsin\left(\frac{R_C + R_\alpha^{(1)}}{R_S + R_\alpha^{(1)}}\right). \tag{20}$$

The energy of the first neck is

$$\begin{aligned}\epsilon_k^{(1)} = \frac{\pi}{2}\kappa&\left[\left(1 + \frac{R_C}{R_\alpha^{(1)}} + \frac{3}{2}\frac{R_\alpha^{(1)}}{R_C} + \frac{1}{2}\left(\frac{R_\alpha^{(1)}}{R_C}\right)^2\right)\theta_0 - \left(3 + 2\frac{R_\alpha^{(1)}}{R_C} + \left(\frac{R_\alpha^{(1)}}{R_C}\right)^2\right)\sin\theta_0 + \frac{1}{4}\frac{R_\alpha^{(1)}}{R_C}\left(3 + \frac{R_\alpha^{(1)}}{R_C}\right)\sin 2\theta_0 + \frac{1}{3}\left(\frac{R_\alpha^{(1)}}{R_C}\right)^2\sin^3\theta_0\right]\\ &- \pi(k_c - 1)\frac{R_\alpha^{(1)}}{R_C}\left[\frac{1}{2}\left(1 + \frac{R_\alpha^{(1)}}{R_C}\right)\theta_0 - \frac{1}{4}\left(1 + \frac{R_\alpha^{(1)}}{R_C}\right)\sin 2\theta_0 - \frac{R_\alpha^{(1)}}{3R_C}\sin^3\theta_0\right]\\ &- \pi c_0^* R_\alpha^{(1)}\left[\left(1 + \frac{R_C}{R_\alpha^{(1)}} - \frac{1}{2}\frac{R_\alpha^{(1)}}{R_C}\right)\theta_0 + \frac{R_\alpha^{(1)}}{R_C}\sin\theta_0 - \frac{R_\alpha^{(1)}}{4R_C}\sin 2\theta_0\right],\end{aligned} \tag{21}$$

and its area

$$A_k^{(1)} = 2\pi R_\alpha^{(1)}\left[\left(R_\alpha^{(1)} + R_C\right)\theta_0 - R_\alpha^{(1)}\sin\theta_0\right]. \tag{22}$$

The second neck has to join the cylinder smoothly to a flat membrane, thus $\alpha_{max}^{(2)} = \pi/2$, and as before, $R_\beta{}^{(2)} = R_C$ (Fig. 9). The domain boundary has a length $2\pi(R_\alpha{}^{(2)} + R_C)$. The energy of the second neck is

$$\begin{aligned}\epsilon_k^{(2)} = \frac{\pi}{2}\kappa&\left(\frac{\pi}{2}\frac{R_C}{R_\alpha^{(2)}} + \left(\frac{3\pi}{4} - 2\right)\frac{R_\alpha^{(2)}}{R_C} + \left(\frac{\pi}{4} - \frac{2}{3}\right)\left(\frac{R_\alpha^{(2)}}{R_C}\right)^2 + \frac{\pi}{2} - 3\right) - \pi(k_c - 1)\frac{R_\alpha^{(2)}}{R_C}\left(\frac{\pi}{4} + \left(\frac{\pi}{4} - \frac{1}{3}\right)\frac{R_\alpha^{(2)}}{R_C}\right)\\ &- \pi c_0^* R_\alpha^{(2)}\left(\frac{\pi}{2} + \frac{\pi}{2}\frac{R_C}{R_\alpha^{(2)}} + \left(1 - \frac{\pi}{4}\right)\frac{R_\alpha^{(2)}}{R_C}\right) + 2\pi(R_\alpha^{(2)} + R_C),\end{aligned} \tag{23}$$

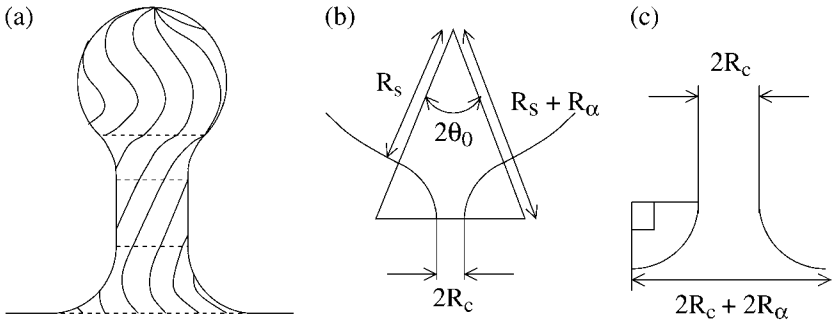

FIGURE 9 (*a*) Texture of a flask, horizontal dashed lines mark out the two necks, (*b*) geometry of the neck connecting the spherical to the cylindrical part of the flask, (*c*) geometry of the neck connecting the cylindrical part of the flask to the rest of the membrane.

and its area

$$A_k^{(2)} = 2\pi R_\alpha^{(2)}\left[\left(\frac{\pi}{2}-1\right)R_\alpha^{(2)} + \frac{\pi}{2}R_C\right]. \tag{24}$$

The total energy of the flask can now be written as,

$$E_{flask} = \epsilon_k^{(2)} + 2\pi R_C L_C\left(\frac{\kappa}{4R_C^2} - \frac{c_0^*}{2R_C}\right) + \epsilon_k^{(1)} + 2\pi\kappa(1+\cos\theta_0) - \pi(k_c-1)\int_{\theta_c}^{\pi-\theta_0}\frac{\cos^2\theta}{\sin\theta}d\theta + \epsilon_c, \tag{25}$$

where L_C is the length of the cylinderical part and θ_0 is given by Stryer (20). We have numerically obtained the optimum shape of the flask (i.e., the values of $\{R_S, R_C, R_\alpha{}^{(1)}, R_\alpha{}^{(2)}, L_C\}$ that minimize E_{flask}), subject to the constraint of constant total area,

$$A = \pi R^2 = A_k^{(1)} + A_k^{(2)} + 2\pi R_S^2(1+\cos\theta_0) + 2\pi R_C L_C. \tag{26}$$

The optimal shapes fall into two broad classes (Fig. 10): (*A*) a spherical bud, with no neck, i.e., $L_C = 0$, and (*B*) a flask shape, with $L_C > 0$. Every bud has $R_\alpha^{(1)} \ll R_S$ and $R_\alpha^{(2)} \ll R_S$, while every flask has $R_\alpha^{(1)} \ll R_S$ and $R_\alpha^{(2)} \ll L_C$.

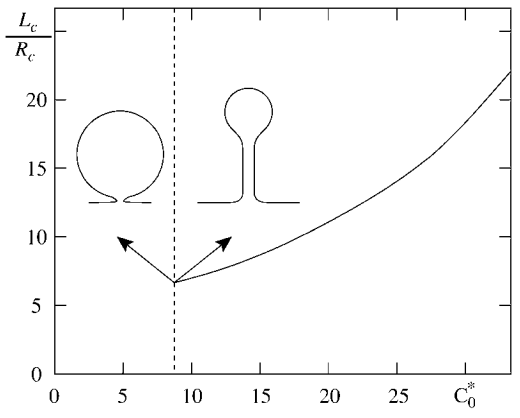

FIGURE 10 Discontinuous transition from spherical bud to flask ($k_c = 2$, $R = 5$). To the left of the broken line $L_C = 0$, the optimum shape is a bud. Inset shows the optimum shapes (to scale) on either side of the transition (*dashed line*).

Therefore the necks are narrow and the shape of the flask is almost entirely determined by the dimensions of the spherical and the cylindrical parts.

We now study how changing c_0^*, R, and κ affect the shape parameters of the flask. For fixed values of R, k_c, and κ, flask shapes are obtained only when the chiral strength c_0^* crosses a threshold, any smaller value will produce only a bud (Fig. 10). This threshold c_0^* increases with increase in k_c (Fig. 11). More interestingly, the threshold c_0^* decreases with an increase in R (Fig. 11), implying that larger (stable) domains favor flask formation. Thus for a given k_c and c_0^*, there is a minimum size, R_{min}, for a raft to be a flask (Fig. 12), consistent with observations of caveolae supporting cells. The transition from bud to flask is discontinuous—keeping R and k_c fixed, the length of the cylindrical part jumps sharply from zero beyond a threshold c_0^* (Fig. 10).

We comment on the dependence of the flask shape parameters on the bending stiffness κ. As seen from Fig. 12, the minimum size of a domain capable of taking the shape of a flask, R_{min}, increases with κ, for fixed values of k_c and c_0^*. Thus a large κ favors the formation of flask-shaped caveolae. This is consistent with an expected stiffening of the caveolar membrane with its associated bound caveolin oligomers.

As mentioned earlier, we have shown that the flask morphology is favorable under conditions of: i), high chiral strength k_c and c_0^*; ii), large raft area R; and iii), high bending modulus κ—conditions that are characteristically met in caveolae.

Grapes of raft

If the area of the domain becomes sufficiently large then the competition between k_c and c_0^* would produce an optimal combination of spheres (with the lines of **m** bunched into tight spirals toward the poles), and cylinders (with the lines of **m** wrapped in a helical texture). This produces the grape-like structures seen in caveolae—a string of spherical bulbs connected by a system of tubules (Fig. 13).

We extend the shape parameterization to include spheres (S_1, S_2, S_3, ...) connected to cylinders (T_1, T_2, T_3, ...) by saddles (N_1, N_2, N_3, ...) with the whole structure joining the rest of the membrane through a neck N_0 (Fig. 13). Each of these components has exactly the same texture as the

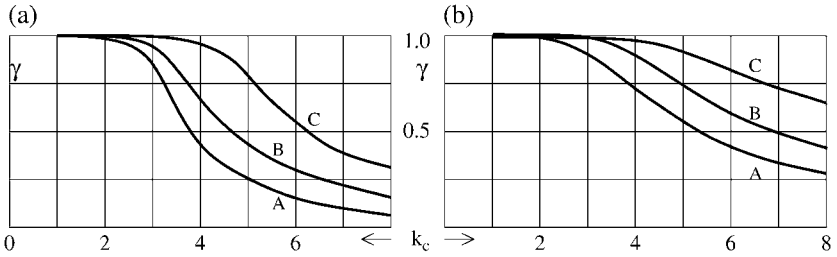

FIGURE 11 Variation of flask shape parameter $\gamma = R_C/R_S$ with chiral strengths κ_c and c_0^*. Plots show γ vs. κ_c for different c_0^* (*a*) $R = 5$ and $c_0^* = 40$ (*A*), 50 (*B*), 60 (*C*); (*b*) $R = 3$ and $c_0^* = 60$ (*A*), 70 (*B*), 80 (*C*). Rest of the parameters are $\kappa = 10$, $r_c = 0.05$, $\epsilon_c = 0$.

flask-shaped caveola. For simplicity, we take all tubules to be of the same dimension ($\{L_C, R_C\}$), all bulbs to be of the same radius (R_S), and all necks (except N_0) to be of the same outer radius (R_α) and inner radius ($R_\beta = R_C$).

A variational calculation shows that given the values of k_c and c_0^*, the optimal number of bulbs and tubules in the grape-like structures increases with the domain size R and the stiffness κ (Fig. 14). Furthermore, for fixed R and κ, the number of bulbs reduces and the tubules get longer, as c_0^* increases. There is a threshold c_0^* in order for the grape structure to have any tubular part at all—a smaller c_0^* leads to $L_C = 0$ and the membrane takes the form of a necklace of spherical buds connected by infinitely narrow necks.

ESTIMATION OF PARAMETERS

Spanning the parameter space gives a whole taxonomy of energy-minimizing shapes; experimental comparison can only be made by fixing the parameter values. Unfortunately these parameter values are not known in the plasma membrane; the best we can do is to obtain values determined in artificial systems resembling the cellular context. For instance, membrane deformation parameters are taken from studies on artificial membranes with reconstituted lipids. Frank elastic parameters are taken from estimates from liquid crystal physics, whereas parameters related to the coupling between the orientational field and membrane curvature should ideally be taken from Sm-*C** films.

The values of membrane elastic parameters, like the bending modulus κ, spontaneous curvature c_0, and the line tension σ_0 have been noted in the section ''Inadequacy of conventional mechanisms of budding of raft components on the cell surface''. Analysis of the thermal fluctuation spectrum of giant (20 μm diameter) quasispherical vesicles containing a mixture of DMPC and cholesterol by phase-contrast video microscopy (60) gives a value of $\kappa = 4 \times 10^{-19}$ J for 50 mol % of cholesterol (resembling the local concentration of cholesterol in the putative rafts) at 40°C. The value of the (global) surface tension in live cells (61) has been estimated as $\gamma \sim 10^{-2}$–10^{-1} pN/nm. The bending modulus and tension in the raft environment of the cell, if anything should be larger than this, both due to binding to cytoskeleton and being in the *lo* state. The line tension of the lipid-raft domain can be obtained via an analysis of shape deformations of lipid domains in Langmuir monolayers (62) or from domain shapes and sizes in phase-segregated GUVs containing the ternary lipid mixture Sph/Chol/PC. These experiments lead to an estimate of $\sigma_0 \sim 10^{-13}$ N for the line tension. A more recent study (29) on giant unilamellar vesicles in which *lo* domains, rich in cholesterol and sphingolipids, coexist with liquid-disordered (*ld*) patches consisting mainly of unsaturated phospholipids, has come up with a value that is an order of magnitude larger than this.

The values of the Frank constants entering the lipid bilayer membrane energy functional, may be obtained from the corresponding values in bulk liquid crystals. In a cholesteric liquid crystal, the director field $\vec{n}$, describing the locally averaged molecular (long) axis, describes a helical conformation about a fixed ordering axis. This helical conformation is best imagined as a set of parallel planes, with $\vec{n}$ at every point in a given plane having the same orientation, while $\vec{n}$ at successive planes twisting with a prescribed pitch around a fixed axis perpendicular to the planes (41). The energy density of this conformation is expressed by the Frank form,

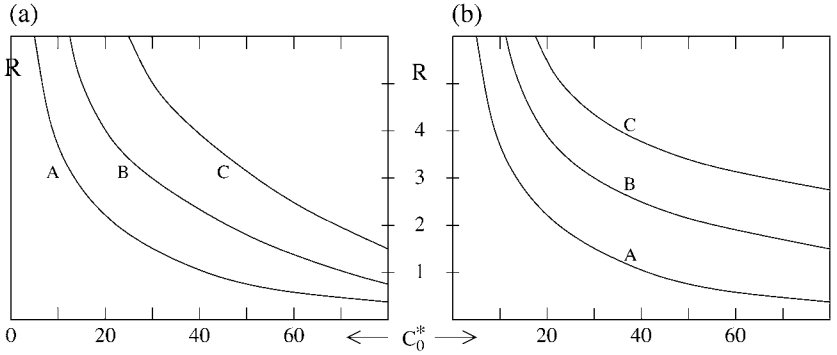

FIGURE 12 Lines separating the bud from the flask in the $R - c_0^*$ plane—to the left (*right*) of each curve is the bud (flask), with $r_c = 0.05$ and $\epsilon_c = 0$: (*a*) $\kappa = 10$ and $k_c = 2$ (*A*), 5 (*B*), 8 (*C*); (*b*) $k_c = 2$ and $\kappa = 10$ (*A*), 20 (*B*), 30 (*C*).

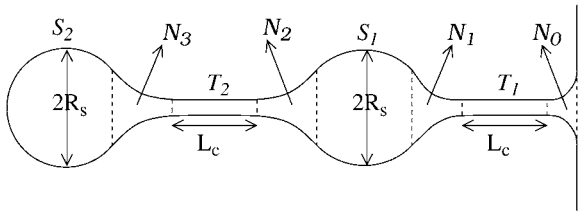

FIGURE 13 String of grapes attached to the mother membrane by the neck N_0 and consisting of two bulbs, each of radius R_S, and two identical tubules, each of length L_C. The necks N_1, N_2, and N_3, connecting the tubules with the bulbs are geometrically identical.

$$\mathcal{E} = \frac{K_1}{2}(\mathrm{div}\,\vec{n})^2 + \frac{K_2}{2}(\vec{n}\cdot\mathrm{curl}\,\vec{n} + q)^2 + \frac{K_3}{2}(\vec{n}\times\mathrm{curl}\,\vec{n})^2, \tag{27}$$

where $2\pi/q$ is the pitch of the helical conformation of $\vec{n}$. Comparing the energy density of a planar tilt domain with that of a cholesteric above, suggests the following correspondence: $k_1 \sim \ell K_1$, and $k_2 \sim \ell K_3$, where the length scale ℓ is of the order of the thickness of the bilayer bearing the raft. Knowing the values of the Frank constants for the bulk cholesteric, $K_1 \sim K_2 \sim K_3 \sim 10^{-11}$ N, and taking $\ell \sim 1$ nm, we arrive at an estimate for the Frank coefficients in the membrane energy functional, $k_1 \sim k_2 \sim 10^{-20}$ J.

The two crucial chiral parameters k_c and c_0^* can also be estimated. Note that $\mathcal{E}$ in Veatch and Keller (27) has a term linear in curl $\vec{n}$; this chiral term is related to the parameter k_c, suggesting that $k_c \sim \ell K_2 \sim 10^{-20}$ J. These values are almost an order of magnitude larger than k_BT at 30°C, and so we may ignore the effect of thermal agitation on the ordering of **m** in a raft.

The other chiral parameter is the Helfrich-Prost c_0^*. Clearly the sign of c_0^* is irrelevant to our discussion; if we obtain a particular energy-minimizing conformation of the decorated membrane with a positive value of c_0^*, then reversing the sign of c_0^* would only reverse the handedness of the texture on the membrane, leaving the shape of the membrane unchanged. The magnitude of c_0^* has not been determined experimentally for any system, including Sm-C^* films. A crude upper limit can be obtained from a theoretical estimate (53); because c_0^* has dimensions of inverse length, one gets an upper bound of order 10^3 (in our dimensionless units) if we take that length to be ℓ. The value of c_0^* we need to form buds and tubules is well within this bound.

With these parameter estimates, we now argue post facto that long-ranged dipolar interactions are significantly weaker than the Frank contributions. Sphingolipids have a dipole moment $|\vec{p}|\sim 1$ debye (22) directed roughly parallel to the plane of the membrane and at the same level as the bridge group (almost touching the interface of the hydrocarbon chains and water). The strength of dipolar interactions of neighboring sphingolipids is of the order $|\vec{p}|^2/a^3$ where $a \sim 1$ nm is the separation of the lipid dipoles. This energy is of order 10^{-22} J, as a result, dipolar interactions cannot perturb the order imposed on **m** by the Frank energy. On the other hand, GPI-anchored proteins are anionic, thus the strength of electrical interaction is considerably enhanced $|\vec{p}|q/a^2 \sim 10^{-20}$ J for $q = 1$ Coulomb and $a \approx 0.8$ nm. The charged lipid would then be shielded by a dipole cloud with each dipole pointing radially into the charge, impairing the order of **m** created by the Frank energy (this charge-dipole interaction can be made considerably weaker by the presence of dissolved counterions).

OTHER SIMPLE TESTABLE CONSEQUENCES OF CHIRALITY-INDUCED BUDDING

We briefly discuss some simple testable consequences of chirality-induced budding, in addition to those described in

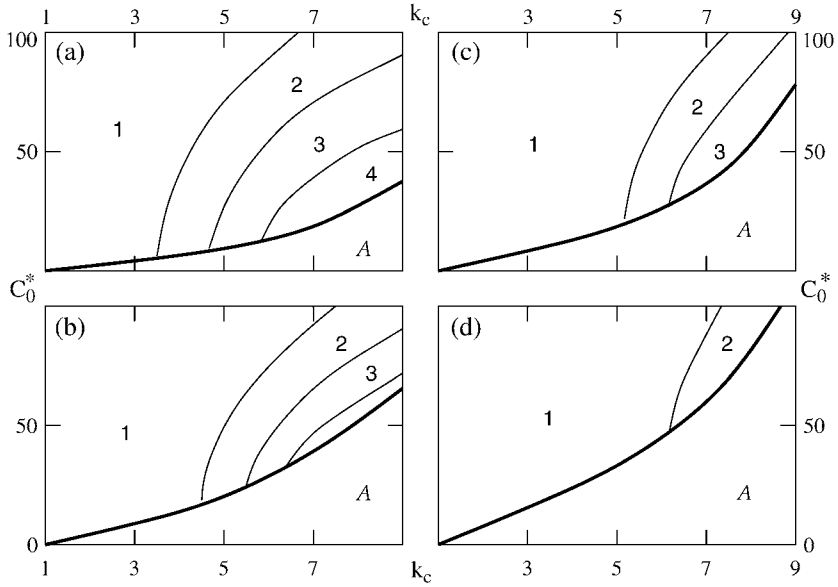

FIGURE 14 Optimum shape of grapes with n bulbs connected by n tubules in the $k_c - c_0^*$ plane. The label (*1*, *2*, *3*) in each panel refers to the optimum value of n, whereas in the region marked A there is no tubule: (*a*) $R = 5, \kappa = 10$; (*b*) $R = 5, \kappa = 20$; (*c*) $R = 3, \kappa = 10$; (*d*) $R = 3, \kappa = 20$.

earlier sections. First note that the variational shapes of the membrane buds that we explored are not explicitly chiral. Examples of such explicit chiral shapes are the twisted ribbons (46,47) and helical tubules. Observation of such shapes in multicomponent membrane systems would immediately imply a coupling of chirality to curvature. We are currently extending our variational calculation to check whether such helical tubules are energy-minimizing shapes within our model.

We have shown that the microscale segregation of specific lipids possessing chirality and tilt can lead to membrane deformation such as budding or tubulation. We now ask the converse question—can local curvature enhancement, either via budding/tubulation or thermal/active fluctuations, result in the recruitment of chiral/tilt molecules from the surrounding membrane (63)? We answer in the affirmative.

The calculation broadly follows along the lines of Leibler and Andelman (64). Consider a bilayer membrane composed of two distinct kinds of lipids: a majority component comprising (for example) DMPC in the *ld* phase, whereas the minority component composed of lipids such as DPPC/Chol (or even Sph/Chol) in the *lo′* phase. Recall that we have already introduced the *lo′* phase in the section ''Rafts: a membrane patch involving orientation and chirality''; it is the tilt version of the *lo* phase, and is characterized both by high packing fraction (and consequent chain stiffening) and molecular tilt. We prepare the membrane in the mixed phase, in the neighborhood of the *ld*-*lo′* phase boundary, and ask whether curvature deformations can induce phase segregation of the chiral/tilt component. For this we need to write the energy functional in ϕ, the relative concentration of the chiral/tilt species,

$$
\begin{aligned}
E[\phi,\mathbf{m},\vec{R}] = \int \sqrt{g}d^2x\Big\{ & \left[\frac{c}{2}(\nabla\phi)^2+\frac{a}{2}\phi^2+c_0(\phi)H+\frac{\kappa}{2}H^2+\frac{\bar{\kappa}}{2}K\right] \\
& +\phi\left[\frac{k_1}{2}(\mathrm{Div}\,\mathbf{m})^2+\frac{k_2}{2}(\mathrm{Curl}\,\mathbf{m})^2+k_c(\mathrm{Div}\,\mathbf{m})(\mathrm{Curl}\,\mathbf{m})+\sigma_1(\mathrm{Div}\,\mathbf{m})+\sigma_2(\mathrm{Curl}\,\mathbf{m})\right] \\
& +\phi\left[\beta m^i m^j K^i_j + c_0^* \gamma_{ij} m^k m^i K^j_k\right]\Big\},
\end{aligned}
\tag{28}
$$

where $a \propto (T - T_c) > 0$, is the deviation from the demixing temperature. It is clear from Veatch and Keller (28) that both the coupling of ϕ to: i), curvature via c_0, and ii), curvature via tilt and chirality, renormalize a to negative values, inducing phase segregation.

This curvature induced segregation can be realized by using optical tweezers to pull tubules from GUVs made from a mixture of appropriate lipids. Pulling a tether in the mixed phase would induce phase segregation, with the chiral/tilt components (*lo′* phase) preferentially partitioning in the tubule. Note that this is the opposite of what happens when the binary lipid mixture is composed of lipids exhibiting the *lo* and *ld* phases; in this case, too, pulling a tether in the mixed phase induces phase segregation, however, it is the *ld* phase that preferentially partitions into the tubule (65). The width of the tubule is given by $\sqrt{\kappa/\gamma}$, where κ and γ are the renormalized bending modulus and tension, respectively. Because the renormalized κ and γ are different in the two phases, the width of the tubule is a good measure of which phase partitions in the tubule.

DISCUSSION AND EXTENSION TO OTHER CELLULAR CONTEXTS

Membrane budding in cells has been hypothesized to occur via a variety of means. Although both specific lipids and proteins have been reported as key players in providing the requisite membrane deformation forces leading to budding, there is little understanding of the physical mechanisms by which this process occurs in cellular systems. In the context of raft-mediated budding, associated with the internalization of GPI-anchored proteins, we have argued that local membrane deformation is a result of the special lipid character of rafts. We have shown that conventional mechanisms that invoke line tension, arising from lateral compositional heterogeneity, and spontaneous curvature, arising from bilayer compositional asymmetry cannot account for the small size ($\approx$50 nm radius) and the varied shapes (spheres, tubules, flasks, and grapes) of raft-associated budding in GPI-anchored protein endocytosis and the stable caveolae. In this article we propose another mechanism for budding that invokes molecular features specific to raft lipids such as sphingolipids and cholesterol, namely, tilt and chirality. We argue that the interplay between tilt, chirality, and local membrane curvature, can induce membrane budding. This chirality-induced budding accounts for both the small size and the variety of shapes exhibited by raft-associated buds and caveolae. Indeed, the qualitative features of membrane budding that we describe is consistent with the special characteristics of caveolae.

One direct consequence of chirality is the tendency of large domains to split. In our view, this has important cellular implications; large domains can only be maintained by ''stitching up'' smaller ones together. We suggest that caveolin oligomerization and binding, in addition to its possible role in providing membrane bending moments, may act to hold

the raft constituents together. This suggestion is a radically new proposal for the role of coat proteins such as caveolin. Membrane bound caveolin also provides a spontaneous curvature and a larger bending stiffness κ, features that favor flask and grape-like morphologies, often associated with caveolar structures in mammalian cells.

We point out one more phenotype that emerges naturally from our model. Oligomerized and membrane-bound caveolin is a semiflexible polymer attached to the deformable membrane. Recent evidence for this notion comes from filamentous structures adopted by caveolin oligomers in vitro (58). The local tangent vector associated with this semiflexible polymer will couple to the curvature in exactly the same way as the tilt vector, and thus appear in the Hamiltonian in exactly the same form as **m**, albeit with different parameter values. This would immediately imply that the backbone of the caveolin oligomers will trace out helical lines on the membrane bud (akin to the lines of **m**). This would explain the geometry of the striations observed in electron microscopy pictures of caveolae (59,67).

Thus far we have discussed the possible involvement of a novel membrane budding mechanism involving molecular tilt and chirality, in raft-mediated endocytosis and caveolae. In this section we inquire whether this mechanism may also be involved in other pathways, such as the clathrin-mediated endocytic pathway. After all chirality and tilt are molecular properties shared both by lipids and proteins, and so it is conceivable that different endocytic pathways may utilize this common theme using different molecular players.

One of the molecular players involved in the clathrin-mediated endocytic pathway is the Epsin family of proteins, such as Epsin I and II. Recent experiments on live cells and reconstituted freely suspended bilayers (6) have shown the direct involvement of Epsin in membrane curvature generation leading to budding. It was found that Epsin, a multidomain protein, undergoes a specific conformational change upon binding with clathrin; this involves a long α-helix arm, which being amphipathic lies on the plane of the inner leaflet of the plasma membrane. We suggest that the capacity of Epsin to induce membrane budding is related to the chirality and tilt of this α-helix domain.

Our parameter estimates suggest that such chirality-induced budding should be observed in membranes containing generic lipids and/or proteins as long as they can be described by a tilt and chirality. Recall that for this mechanism to be operative, both tilt and chirality have to be expressed over large scales. This, as has been discussed, are features exhibited in specific regions of the cell surface such as ''rafts''.

APPENDIX A: FORMULAS FOR THE CALCULATION OF ENERGY

To be self-contained, we give here a compendium of known differential geometric formulas, needed for the computation of the mechanical energy of the membrane. We follow the notation of David (68).

Any point on the surface of the membrane is specified by the three-dimensional vector $\vec{R}(x_1, x_2)$, where $x \equiv (x_1, x_2)$ forms a 2D manifold. The tangent plane at any point on the surface is defined by the two covariant vectors $\vec{e}_i = \partial\vec{R}/\partial x^i$ where $i = 1, 2$. The unit normal to this tangent plane is

$$\vec{N} = \frac{\vec{e}_1 \times \vec{e}_2}{|\vec{e}_1 \times \vec{e}_2|}, \tag{A1}$$

whereas the metric tensor is

$$g_{ij} = \vec{e}_i \cdot \vec{e}_j. \tag{A2}$$

With the help of the metric tensor and its inverse, obtained via the definition, $g^{ij}g_{jk} = \delta^i_k$ (summing over repeated indices), we can convert any covariant tensor into its contravariant form, e.g., $\vec{e}^i = g^{ij}\vec{e}_j$. Moreover g_{ij} is needed to take traces and construct symmetric combinations on the curved manifold. We will also need an antisymmetric tensor γ_{ij}, defined as,

$$\gamma_{ij} = (\vec{e}_i \times \vec{e}_j) \cdot \vec{N}, \tag{A3}$$

to take determinants and construct antisymmetric combinations on the curved manifold.

The invariant surface area element bounded by the sides dx_1 and dx_2, used in Nossal (5), is $dA = \sqrt{g}dx_1dx_2$, where $g = \det g_{ij}$.

The curvature tensor is defined as,

$$K_{ij} = \vec{N} \cdot \frac{\partial^2\vec{R}}{\partial x^i \partial x^j}; \tag{A4}$$

the trace $H = g_{ij}K_{ij}$ and the determinant $K = \gamma_{ij}K_{il}K_{lj}$ of the curvature tensor are the mean and intrinsic (Gaussian) curvatures, respectively.

The Frank terms (4) contain derivatives of scalars and vectors on the curved manifold. We define the gradient of a scalar field ϕ by the covariant tensor,

$$\mathrm{Grad}\phi = \frac{\partial\phi}{\partial x^i}\vec{e}^i. \tag{A5}$$

To define derivatives (divergence and curl) of a vector field $\vec{m}$ on the tangent plane, we first decompose it into its tangent plane components

$$\vec{m} = m_i\vec{e}^i, \tag{A6}$$

and then define the covariant derivative acting on the components of this vector field,

$$D_i m^k = \frac{\partial m^k}{\partial x^i} + \Gamma^k_{ij}m^j, \tag{A7}$$

where Γ^k_{ij} is called the connection,

$$\Gamma^k_{ij} = \vec{e}^k \cdot \frac{\partial\vec{e}_j}{\partial x^i}. \tag{A8}$$

The divergence and curl of $\vec{m}$ is now defined as,

$$\mathrm{Div}\,\vec{m} \equiv D_i m^i \tag{A9}$$

$$\mathrm{Curl}\,\vec{m} \equiv \gamma^j_i D_i m^j. \tag{A10}$$

Armed with these formulas, we can calculate each of the terms appearing in the energy functional (2) for any vector field on an arbitrary prescribed surface. Because any small chip off a surface can be approximated by a plane, a sphere, a cylinder, or a saddle (52), we present explicit formulas for these surfaces (Fig. 15):

(i) Sphere $\quad \vec{R} \equiv (r\cos\theta\sin\phi, r\sin\theta\sin\phi, r\cos\phi)$:

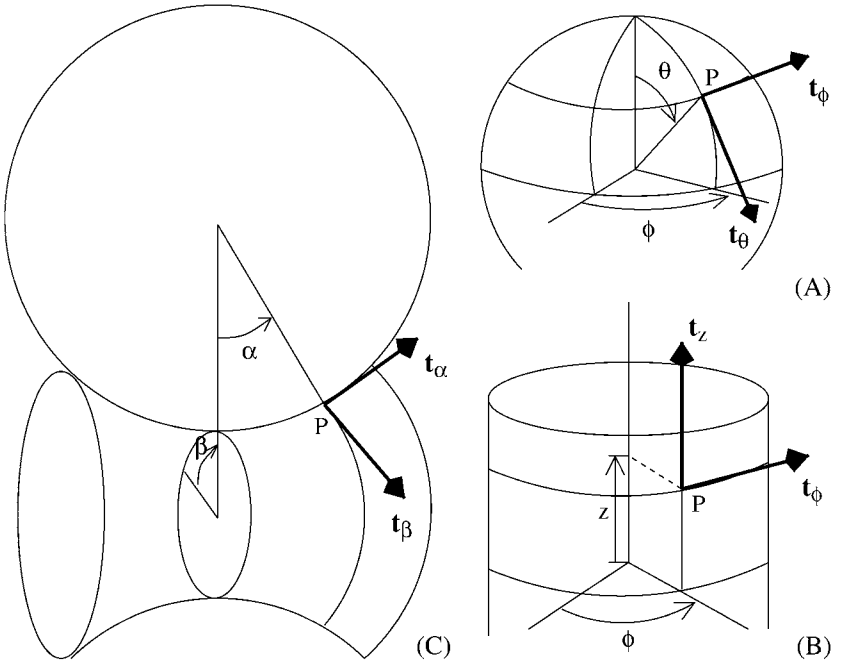

FIGURE 15 Local coordinate systems and tangent basis on three elementary surfaces: (*A*) sphere, (*B*) cylinder, (*C*) saddle.

$$g_{11} = r^2,\ g_{12} = 0,\ g_{21} = 0,\ g_{22} = r^2\sin^2\theta \tag{A11}$$

$$K_1^1 = \frac{1}{r},\ K_1^2 = 0,\ K_2^1 = 0,\ K_2^2 = \frac{1}{r} \tag{A12}$$

$$\mathrm{Div}\,\vec{m} = \frac{1}{r}\frac{\partial m_\theta}{\partial\theta} + \frac{1}{r\sin\theta}\frac{\partial m_\phi}{\partial\phi} + \frac{\cot\theta}{r}m_\theta \tag{A13}$$

$$\mathrm{Curl}\,\vec{m} = \frac{1}{r}\frac{\partial m_\phi}{\partial\theta} - \frac{1}{r\sin\theta}\frac{\partial m_\theta}{\partial\phi} + \frac{\cot\theta}{r}m_\phi. \tag{A14}$$

(ii) Cylinder $\vec{R} \equiv (r\cos\phi, r\sin\phi, z)$:

$$g_{11} = r^2,\ g_{12} = 0,\ g_{21} = 0,\ g_{22} = 1 \tag{A15}$$

$$K_1^1 = \frac{1}{r},\ K_1^2 = 0,\ K_2^1 = 0,\ K_2^2 = 0 \tag{A16}$$

$$\mathrm{Div}\,\vec{m} = \frac{1}{r}\frac{\partial m_\phi}{\partial\phi} + \frac{\partial m_z}{\partial z} \tag{A17}$$

$$\mathrm{Curl}\,\vec{m} = \frac{1}{r}\frac{\partial m_z}{\partial\phi} - \frac{\partial m_\phi}{\partial z}. \tag{A18}$$

(iii) Saddle $\vec{R} \equiv ((R_\beta + R_\alpha(1-\cos\alpha))\cos\beta,\ (R_\beta + R_\alpha(1-\cos\alpha))\sin\beta, R_\alpha\sin\alpha)$:

$$g_{11} = R_\alpha^2,\ g_{12} = 0,\ g_{21} = 0,\ g_{22} = R_\beta^2 \tag{A19}$$

$$K_1^1 = \frac{1}{R_\alpha},\ K_1^2 = 0,\ K_2^1 = 0,\ K_2^2 = -\frac{\cos\alpha}{R_\beta} \tag{A20}$$

$$\mathrm{Div}\,\vec{m} = \frac{1}{R_\alpha}\frac{\partial m_\alpha}{\partial\alpha} + \frac{1}{R_\beta}\frac{\partial m_\beta}{\partial\beta} + \frac{\sin\alpha}{R_\beta}m_\alpha \tag{A21}$$

$$\mathrm{Curl}\,\vec{m} = \frac{1}{R_\alpha}\frac{\partial m_\beta}{\partial\alpha} - \frac{1}{R_\beta}\frac{\partial m_\alpha}{\partial\beta} + \frac{\sin\alpha}{R_\beta}m_\beta. \tag{A22}$$

APPENDIX B: UNDERSTANDING THE CHIRAL TEXTURE-SHAPE COUPLING

We will illustrate the meaning of the chiral terms in the energy functional (5) in a few simple cases. We will see how these terms lead to textures on a surface that can never be made to coincide with its mirror image no matter where we place the mirror. Any small chip off a surface can be approximated by a plane, a sphere, a cylinder, or a saddle (52). We will ignore the plane, since any texture drawn on a plane is achiral. First note that none of these elementary surfaces is chiral. Thus we will place the mirror so that the bare surface (stripped of its texture, **m**) coincides with its reflection. Then we will decorate the surface, looking for a texture that maximizes the contribution of the chiral terms.

Chiral texture on a sphere

Any point on a sphere is specified by the colatitude θ and longitude ϕ (Fig. 15 *A*). The tangent plane at any point on it is framed by the unit vectors $\mathbf{t}_\theta$ (along the direction of increasing θ and constant ϕ) and $\mathbf{t}_\phi$ (along the direction of increasing ϕ and constant θ). The texture at any point is defined by

$$\mathbf{m} = m_\theta\mathbf{t}_\theta + m_\phi\mathbf{t}_\phi \tag{B1}$$

$$m_\theta^2 + m_\phi^2 = 1. \tag{B2}$$

Any mirror passing through the center will leave the sphere unchanged after reflection; we therefore place the mirror along the arc *BAC* (Fig. 16) where *A* is the pole ($\theta = 0$). If the texture consists of great circles diverging from the pole, $m_\theta = 1$, $m_\phi = 0$ (Fig. 16 *A*) or lines ''parallel'' to the equator, $m_\theta = 0$,

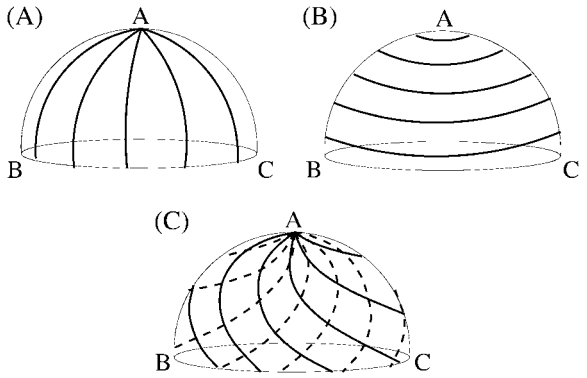

FIGURE 16 Textures (*solid lines*) on a sphere and their reflection (*dashed lines*) on a mirror that lies on the plane of the article (containing the arc *BAC*). (*A*) Lines are great circles diverging from the pole, (*B*) lines are ''parallel'' to the equator, (*C*) lines obliquely cut circles of latitude and longitude; the mirror image cannot be superimposed on itself.

$m_\phi = 1$ (Fig. 16 *B*), then its mirror image coincides with itself, and so gives no contribution to the chiral terms. However, if the texture consists of lines obliquely cutting the circles of latitude and longitude everywhere on the sphere (Fig. 16 *C*), then it is impossible to superpose its mirror image on itself. In fact we expect the chiral term to be greatest when the lines at every point bisect the right angle formed by the intersection of the circles of latitude and longitude, since under these conditions the lines of the image will deviate most strongly from the lines in the original texture (they will cut each other at right angles).

We calculate the contribution that this texture makes to the two chiral terms in the energy functional (5). The Helfrich-Prost term, $c_0^*\gamma_{ij}m^i m^k K_k^j = 0$, for any texture on the sphere. The chiral term k_c is however nonzero; taking m_θ and m_ϕ to be constant, we get

$$k_c(\mathrm{Div}\,\mathbf{m})(\mathrm{Curl}\,\mathbf{m}) = k_c\left(\frac{\cot\theta}{r}\right)^2 m_\theta m_\phi, \qquad \text{(B3)}$$

where r is the radius of the sphere. The term vanishes when either m_θ or m_ϕ vanishes (Fig. 16, *A* and *B*) and is greatest when $m_\theta = m_\phi = 1/\sqrt{2}$ (Fig. 16 *C*), in accordance with our description above.

Chiral texture on a cylinder

Any point on the cylinder is specified by its altitude z from a reference plane perpendicular to the axis of the cylinder and by its longitude ϕ from a reference plane containing the axis (Fig. 15 *B*). The local tangent plane on the cylinder is defined by the unit vectors $\mathbf{t}_z$ (along increasing z, ϕ being constant) and $\mathbf{t}_\phi$ (along increasing ϕ, z being constant). The texture is

$$\mathbf{m} = m_z\mathbf{t}_z + m_\phi\mathbf{t}_\phi \qquad \text{(B4)}$$

$$m_z^2 + m_\phi^2 = 1. \qquad \text{(B5)}$$

The surface is unchanged by reflection along any mirror containing the axis; we therefore place the mirror on the plane of the paper containing the axis and the line *AB* on the cylinder (Fig. 17). (Note that were we to choose the mirror plane to be perpendicular to the axis, we would arrive at the same conclusions.). Clearly, if the texture consists of lines parallel to the axis, $m_z = 1, m_\phi = 0$ (Fig. 17 *A*) or perpendicular to it, $m_z = 0, m_\phi = 1$ (Fig. 17 *B*), then its mirror image coincides with itself. These textures cannot contribute to the chiral terms. The chiral term would be greatest when the lines are inclined to the axis at $\pi/4$, since under this condition, the lines of the image deviate greatest from those of the original (they cut each other at right angles).

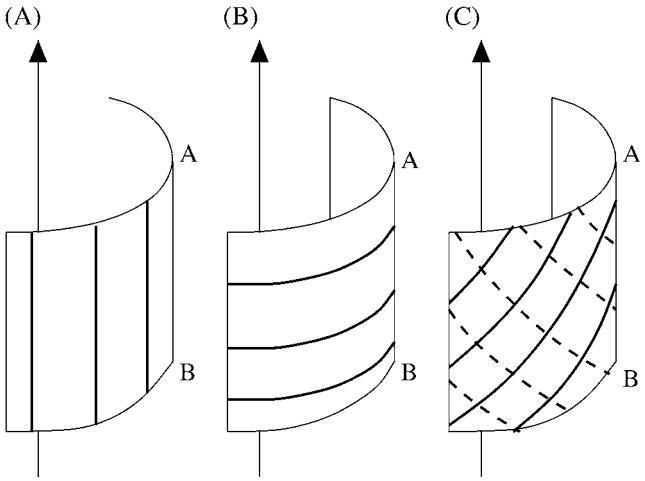

FIGURE 17 Textures (*solid lines*) on a cylinder and their reflection (*dashed lines*) on a mirror that lies on the plane of the article (containing the axis and the edge *AB*). (*A*) Lines parallel to the axis, (*B*) lines perpendicular to the axis, (*C*) lines inclined to the axis; the mirror image cannot be superimposed on itself.

We now calculate the chiral energy terms for these textures. Taking m_z and m_ϕ to be constant, we find that $k_c(\mathrm{Div}\,\mathbf{m})(\mathrm{Curl}\,\mathbf{m}) = 0$, whereas the Helfrich-Prost term

$$c_0^*\gamma_{ij}m^i m^k K_k^j = c_0^*\left(\frac{1}{r}\right)m_z m_\phi, \qquad \text{(B6)}$$

where r is the radius of the cylinder. This term vanishes if either component of $\mathbf{m}$ vanishes (Fig. 17, *A* and *B*), and is maximum when $m_z = m_\phi = 1/\sqrt{2}$ (Fig. 17 *C*). Observe that the texture with equal and constant components of $\mathbf{m}$ is a helix, and that the Helfrich-Prost term is inversely proportional to r. Therefore a large value of c_0^* would wrap $\mathbf{m}$ in a helix around a narrow tube, the pitch of the helix being proportional to the radius of the tube. The same effect of molecular chirality on the shape of tilted fluid bilayer membranes, anisotropic solid membranes, and ferroelectric liquid crystals has been described in Helfrich and Prost (49).

Chiral texture on a saddle

Like a cylinder, a saddle, too, has an axis of symmetry; we choose a plane $\mathcal{P}_\alpha$ bearing this axis and place the mirror on it (Fig. 16 *C*). Unlike a cylinder, however, there is only one plane of symmetry that is perpendicular to this axis, call it $\mathcal{P}_\beta$. *B* is the point on the saddle common to $\mathcal{P}_\alpha$ and $\mathcal{P}_\beta$ (Fig. 18); the other common point, opposite to *B*, is on the half of the saddle not shown in the figure. For simplicity we will assume that the lines of intersection of the surface with $\mathcal{P}_\alpha$ and $\mathcal{P}_\beta$ are circles: call them $\mathcal{C}_\alpha$ and $\mathcal{C}_\beta$, respectively. Any point on the surface is specified by α and β, angles of rotation measured from fixed reference points over $\mathcal{C}_\alpha$ and $\mathcal{C}_\beta$, respectively. (For instance, $\alpha = 0$ at any point on $\mathcal{C}_\beta$, and likewise any point on $\mathcal{C}_\alpha$ has a fixed value of β.). In Fig. 15 *C* we define the tangent plane constructed from $\mathbf{t}_\alpha$ and $\mathbf{t}_\beta$ and locally describe any texture on the saddle as

$$\mathbf{m} = m_\alpha\mathbf{t}_\alpha + m_\beta\mathbf{t}_\beta \qquad \text{(B7)}$$

$$m_\alpha^2 + m_\beta^2 = 1. \qquad \text{(B8)}$$

As before, if the texture consists of lines lying on planes passing through the axis, $m_\alpha = 1, m_\beta = 0$ (Fig. 18 *A*) or lines parallel to $\mathcal{P}_\beta$, $m_\alpha = 0, m_\beta = 1$ (Fig. 18 *B*), then they are symmetric with respect to reflection on $\mathcal{P}_\alpha$. These

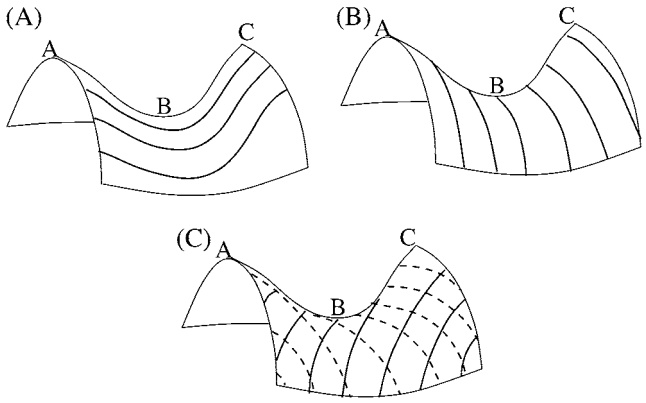

FIGURE 18 Textures (*solid lines*) on a saddle and their reflection (*dashed lines*) on a mirror that bisects the saddle along the line *ABC* and is normal to the surface at *B*. (*A*) Lines lie on planes passing through the axis, (*B*) lines parallel to $\mathcal{P}_\beta$, (*C*) lines bisect the angle between $\mathbf{t}_\alpha$ and $\mathbf{t}_\beta$; the mirror image cannot be superimposed on itself.

textures cannot contribute to the chiral energy. However the chiral energy would be greatest, when the lines of $\vec{m}$ bisect the angle between $\mathbf{t}_\alpha$ and $\mathbf{t}_\beta$ (Fig. 18 *C*).

We now explicitly calculate the chiral energy terms for these textures. For constant m_α and m_β, the Helfrich-Prost term is given by

$$c_0^* \gamma_{ij} m^i m^k K_k^j = c_0^* \left(\frac{1}{R_\alpha} + \frac{\cos\alpha}{R_\beta} \right) m_\alpha m_\beta, \qquad \text{(B9)}$$

where R_α and R_β are the radii of $\mathcal{C}_\alpha$ and $\mathcal{C}_\beta$, respectively. On the other hand the chiral k_c term goes as,

$$k_c (\mathrm{Div}\,\mathbf{m})(\mathrm{Curl}\,\mathbf{m}) = k_c \left(\frac{\sin\alpha}{R_\beta} \right)^2 m_\alpha m_\beta. \qquad \text{(B10)}$$

The total chiral contribution to the energy is indeed greatest for $m_\alpha = m_\beta = 1/\sqrt{2}$ (Fig. 18 *C*) and is zero when either component of $\mathbf{m}$ is zero (Fig. 18, *A* and *B*).

This work was inspired by experiments carried out in our group and we acknowledge the contributions of R. Varma and P. Sharma, co-workers in the raft-related experimental investigations. We thank Y. Hatwalne, N. V. Madhusudhana, V. A. Raghunathan, and S. Ramaswamy for discussions. We thank V. Malhotra for a very careful reading and suggestions that substantially improved the text.

REFERENCES

1. Hopkins, C. R. 1992. Selective membrane protein trafficking: vectorial flow and filter. *Trends Biochem. Sci.* 17:27–32.
2. Conner, S. D., and S. L. Schmid. 2003. Regulated portals of entry into the cell. *Nature*. 422:37–44.
3. Kirchausen, T., J. S. Bonifacino, and H. Riezman. 1997. Linking cargo to vesicle formation: receptor tail interactions with coat proteins. *Curr. Opin. Cell Biol.* 9:488–495.
4. Slepnev, V. I., and P. de Camilli. 2000. Accessory factors in clathrin-dependent synaptic vesicle endocytosis. *Nat. Rev. Neurosci.* 1:161–172.
5. Nossal, R. 2001. Energetics of clathrin basket assembly. *Traffic*. 2: 138–147.
6. Ford, M. G., I. G. Mills, B. J. Peter, Y. Vallis, G. J. Praefcke, P. R. Evans, and H. T. McMahon. 2002. Curvature of clathrin-coated pits driven by epsin. *Nature*. 419:361–366.
7. Mayor, S., and H. Riezman. 2004. Sorting GPI-anchored proteins. *Nat. Rev. Mol. Cell Biol.* 5:110–120.
8. Nichols, B. J., and J. Lippincott-Schwartz. 2001. Endocytosis without clathrin coats. *Trends Cell Biol.* 11:406–412.
9. Sabharanjak, S., P. Sharma, R. G. Parton, and S. Mayor. 2002. GPI-anchored proteins are delivered to recycling endosomes via a distinct cdc42-regulated, clathrin-independent pinocytic pathway. *Dev. Cell*. 2:411–423.
10. Mayor, S., S. Sabharanjak, and F. R. Maxfield. 1998. Cholesterol-dependent retention of GPI-anchored proteins in endosomes. *EMBO J.* 17:4626–4638.
11. Chatterjee, S., E. R. Smith, K. Hanada, V. L. Stevens, and S. Mayor. 2001. GPI-anchoring leads to sphingolipid dependent retention of endocytosed proteins in the recycling endosomal compartment. *EMBO J.* 20:1583–1592.
12. Varma, R., and S. Mayor. 1998. GPI-anchored proteins are organized in submicron domains at the cell surface. *Nature*. 394:798–801.
13. Sharma, P., R. Varma, R.C. Sarasij, Ira, K. Gousset, G. Krishnamoorthy, M. Rao and S. Mayor. 2004. Nanoscale organization of multiple GPI-anchored proteins in living cell membranes. *Cell*. 166:577–589.
14. Mayor, S., and M. Rao. 2004. Rafts: scale dependent, active lipid organization at the cell surface. *Traffic*. 5:231–240.
15. Simons, K., and E. Ikonen. 1997. Functional rafts in cell membranes. *Nature*. 387:569–572.
16. Harder, T., and K. Simons. 1997. Caveolae, DIGs, and the dynamics of sphingolipid-cholesterol microdomains. *Curr. Opin. Cell Biol.* 9: 534–542.
17. Edidin, M. 2003. Lipids on the frontier: a century of cell-membrane bilayers. *Nat. Rev. Mol. Cell Biol.* 4:414–418.
18. Safran, S. A. 2003. Statistical Thermodynamics of Surfaces, Interfaces and Membranes. Westview Press, Boulder, CO.
19. Brown, D. A., and E. London. 1997. Structure of detergent-resistant membrane domains: does phase separation occur in biological membranes? *Biochem. Biophys. Res. Commun.* 240:1–7.
20. Stryer, L. 1995. Biochemistry. W. H. Freeman & Co., New York.
21. Sarasij, R. C., and M. Rao. 2002. Tilt texture domains on a membrane and chirality induced budding. *Phys. Rev. Lett.* 88:088101–088104.
22. Israelachvili, J. 1998. Intermolecular and Surface Forces. Academic Press, London, UK.
23. van Deurs, B., K. Roepstorff, A. M. Hommelgaard, and K. Sandvig. 2003. Caveolae: anchored, multifunctional platforms in the lipid ocean. *Trends Cell Biol.* 13:92–100.
24. Lipowsky, R. 1993. Domain-induced budding of fluid membranes. *Biophys. J.* 64:1133–1138.
25. Julicher, F., and R. Lipowsky. 1993. Domain-induced budding of vesicles. *Phys. Rev. Lett.* 70:2964–2967.
26. Julicher, F., and R. Lipowsky. 1996. Shape transformation of vesicles with intramembrane domains. *Phys. Rev. E.* 53:2670–2683.
27. Veatch, S. L., and S. L. Keller. 2002. Organization in lipid membranes with cholesterol. *Phys. Rev. Lett.* 89:268101–268104.
28. Veatch, S. L., and S. L. Keller. 2003. Separation of liquid phases in giant vesicles of ternary mixtures of phospholipids and cholesterol. *Biophys. J.* 85:3074–3083.
29. Baumgart, T., S. T. Hess, and W. W. Webb. 2003. Imaging coexisting fluid domains in biomembrane models coupling curvature and line tension. *Nature*. 425:821–824.
30. Turner, M., and P. Sens. 2004. Theoretical model for the formation of caveolae and similar membrane invaginations. *Biophys. J.* 86:2049–2057.
31. Rinia, H. A., M. M. E. Snel, J. P. J. M. van der Eerden, and B. de Kruijff. 2001. Visualizing detergent resistant domains in model membranes with atomic force microscopy. *FEBS Lett.* 501:92–96.
32. Anderson, R. G. W., and K. Jacobson. 2002. A role for lipid shells in targeting proteins to caveolae, rafts, and other lipid domains. *Science*. 296:1821–1825.

33. Sheetz, M. P., and S. J. Singer. 1974. Biological membranes as bilayer couples. A molecular mechanism of drug-erythrocyte interactions. *Proc. Natl. Acad. Sc.* 71:4457–4461.

34. Parton, R. G., and A. A. Richards. 2003. Lipid rafts and caveolae as portals for endocytosis: new insights and common mechanisms. *Traffic*. 4:724–738.

35. Dietrich, C., L. A. Bagatolli, Z. N. Volovyk, N. L. Thompson, M. Levi, K. Jacobson, and E. Gratton. 2001. Lipid rafts reconstituted in model membranes. *Biophys. J.* 80:1417–1428.

36. Karmakar, S., and V. A. Raghunathan. 2003. Cholesterol-induced modulated phase in phospholipid membranes. *Phys. Rev. Lett.* 91:098102–098105.

37. Sankaram, M. B., and T. E. Thompson. 1990. Modulation of phospholipid acyl chain order by cholesterol: a solid-state 2H nuclear magnetic resonance study. *Biochemistry*. 29:10676–10684.

38. Chaikin, P. C., and T. C. Lubensky. 1995. Principles of Condensed Matter Physics. Cambridge University Press, Cambridge, UK.

39. Straley, J. P. 1976. Theory of piezoelectricity in nematic liquid crystals, and of the cholesteric ordering. *Phys. Rev. A.* 14:1835–1841.

40. Harris, A. B., R. D. Kamien, and T. C. Lubensky. 1999. Molecular chirality and chiral parameters. *Rev. Mod. Phys.* 71:1745–1757.

41. de Gennes, P. G., and J. Prost. 1993. The Physics of Liquid Crystals. Clarendon, Oxford, UK.

42. Seifert, U., J. Shillcock, and P. Nelson. 1996. Role of bilayer tilt difference in equilibrium membrane shapes. *Phys. Rev. Lett.* 77:5237–5240.

43. Ouyang, Z.-C., and J.-X. Liu. 1990. Helical structures of tilted chiral lipid bilayers viewed as cholesteric liquid crystals. *Phys. Rev. Lett.* 65:1679–1682.

44. Mackintosh, F. C., and T. C. Lubensky. 1991. Orientational order, topology, and vesicle shapes. *Phys. Rev. Lett.* 67:1169–1172.

45. Nelson, P., and T. Powers. 1992. Rigid chiral membranes. *Phys. Rev. Lett.* 69:3409–3412.

46. Selinger, J. V., and J. M. Schnur. 1993. Theory of chiral lipid tubules. *Phys. Rev. Lett.* 71:4091–4094.

47. Selinger, J. V., F. C. Mackintosh, and J. M. Schnur. 1996. Theory of cylindrical tubules and helical ribbons of chiral lipid membranes. *Phys. Rev. E.* 53:3804–3818.

48. Helfrich, W. 1973. Elastic properties of lipid bilayers: theory and possible experiments. *Z. Naturforsch.* 28c:693–703.

49. Helfrich, W., and J. Prost. 1988. Intrinsic bending force in anisotropic membranes made of chiral molecules. *Phys. Rev. A.* 38:3065–3068.

50. Fournier, J.-B. 1996. Non-topological saddle-splay and curvature instabilities from anisotropic membrane inclusions. *Phys. Rev. Lett.* 76: 4436–4439.

51. Chen, C.-M. 1999. Theory for the bending anisotropy of lipid membranes and tubule formation. *Phys. Rev. E.* 59:6192–6195.

52. Spivak, M. 1970. A Comprehensive Introduction to Differential Geometry, 2nd Ed. Publish or Perish, Houston, TX.

53. Langer, S. A., and J. P. Sethna. 1986. Textures in a chiral smectic liquid-crystal film. *Phys. Rev. A.* 34:5035–5046.

54. Pettey, D., and T. C. Lubensky. 1999. Stability of texture and shape of circular domains of Langmuir monolayers. *Phys. Rev. E.* 59:1834–1845.

55. Sarasij, R. C., and M. Rao. 2006. Chiral tilt texture domains in two dimensions. *Phys. Rev. E.* lanl.arXiv.org/cond-mat/0703182.

56. Fourcade, B., L. Miao, M. Rao, M. Wortis, and R. K. P. Zia. 1994. Scaling analysis of narrow necks in curvature models of fluid lipid-bilayer vesicles. *Phys. Rev. E.* 49:5276–5286.

57. Kurzchalia, T. V., and R. G. Parton. 1999. Membrane microdomains and caveolae. *Curr. Opin. Cell Biol.* 11:424–431.

58. Fernandez, I., Y. Ying, J. Albanesiá, and R. G. W. Anderson. 2002. Mechanism of caveolin filament assembly. *Proc. Natl. Acad. Sc.* 99: 1193–1198.

59. Parton, R. G., and K. Simons. 1995. Digging into caveolae. *Science*. 269:1398–1399.

60. Meleard, P., C. Gerbeaud, T. Pott, L. Fernandez-Puente, I. Bivas, M. D. Mitov, J. Dufourcq, and P. Bothorel. 1997. Bending elasticities of model membranes: influences of temperature and sterol content. *Biophys. J.* 72:2616–2629.

61. Sheetz, M. P., and J. W. Dai. 1996. Modulations of membrane dynamics and cell motility by membrane tension. *Trends Cell Biol.* 6:85–89.

62. Rivieŕe, S., and J. Meunier. 1995. Anisotropy of the line tension and bulk elasticity in two-dimensional drops of a mesophase. *Phys. Rev. Lett.* 74:2495–2498.

63. Seifert, U. 1993. Curvature-induced lateral phase segregation in two-component vesicles. *Phys. Rev. Lett.* 70:1335–1338.

64. Leibler, S., and D. Andelman. 1987. Ordered and curved meso structures in membranes and amphiphilic films. *J. Phys.* (*Paris*). 48:2013–2018.

65. Roux, A., D. Cuvelier, P. Nassoy, J. Prost, P. Bassereau, and B. Goud. 2005. Role of curvature and phase transition in lipid sorting and fission of membrane tubules. *EMBO J.* 24:1537–1545.

66. Reference deleted in proof.

67. Rothberg, K. G., J. E. Heuser, W. C. Donzell, Y. S. Ying, J. R. Glenney, and R. G. W. Anderson. 1992. Caveolin, a protein component of caveolae membrane coats. *Cell.* 68:673–682.

68. David, F. 1988. Geometry and Field Theory of Random Surfaces and Membranes. Jerusalem Winter School. D. R. Nelson, T. Piran, and S. Weinberg, editors. World Scientific, Singapore.